

# SANDIA REPORT

SAND2011-6961  
Unlimited Release  
September, 2011

## Enabling Graphene Nanoelectronics

Stephen W. Howell, Taisuke Ohta, Kevin F. McCarty, Thomas E. Beechem III, Wei Pan, Laura B. Biedermann, Anthony Ross III, Craig M. Nolen and Carlos Gutierrez

Prepared by  
Sandia National Laboratories  
Albuquerque, New Mexico 87185 and Livermore, California 94550

Sandia National Laboratories is a multi-program laboratory managed and operated by Sandia Corporation, a wholly owned subsidiary of Lockheed Martin Corporation, for the U.S. Department of Energy's National Nuclear Security Administration under contract DE-AC04-94AL85000.

Approved for public release; further dissemination unlimited.

Issued by Sandia National Laboratories, operated for the United States Department of Energy by Sandia Corporation.

**NOTICE:** This report was prepared as an account of work sponsored by an agency of the United States Government. Neither the United States Government, nor any agency thereof, nor any of their employees, nor any of their contractors, subcontractors, or their employees, make any warranty, express or implied, or assume any legal liability or responsibility for the accuracy, completeness, or usefulness of any information, apparatus, product, or process disclosed, or represent that its use would not infringe privately owned rights. Reference herein to any specific commercial product, process, or service by trade name, trademark, manufacturer, or otherwise, does not necessarily constitute or imply its endorsement, recommendation, or favoring by the United States Government, any agency thereof, or any of their contractors or subcontractors. The views and opinions expressed herein do not necessarily state or reflect those of the United States Government, any agency thereof, or any of their contractors.

Printed in the United States of America. This report has been reproduced directly from the best available copy.

Available to DOE and DOE contractors from

U.S. Department of Energy  
Office of Scientific and Technical Information  
P.O. Box 62  
Oak Ridge, TN 37831

Telephone: (865) 576-8401  
Facsimile: (865) 576-5728  
E-Mail: [reports@adonis.osti.gov](mailto:reports@adonis.osti.gov)  
Online ordering: <http://www.osti.gov/bridge>

Available to the public from

U.S. Department of Commerce  
National Technical Information Service  
5285 Port Royal Rd.  
Springfield, VA 22161

Telephone: (800) 553-6847  
Facsimile: (703) 605-6900  
E-Mail: [orders@ntis.fedworld.gov](mailto:orders@ntis.fedworld.gov)  
Online order: <http://www.ntis.gov/help/ordermethods.asp?loc=7-4-0#online>



SAND2011-6961  
Unlimited Release  
September, 2011

# Enabling Graphene Nanoelectronics

S. W. Howell, L. B. Biedermann, T. J. Ross, C. M. Nolen  
Rad Hard CMOS Technology Department

T. Ohta, C. Gutierrez  
Surface & Interface Sciences Department

K. F. McCarty  
Materials Physics Department

T. E. Beechem  
Nanomaterials Sciences Department

Wei Pan,  
Semicond Material & Device Sci Department

Sandia National Laboratories  
P.O. Box 5800  
Albuquerque, New Mexico 87185-MS0892

## Abstract

Recent work has shown that graphene, a 2D electronic material amenable to the planar semiconductor fabrication processing, possesses tunable electronic material properties potentially far superior to metals and other standard semiconductors. Despite its phenomenal electronic properties, focused research is still required to develop techniques for depositing and synthesizing graphene over large areas, thereby enabling the reproducible mass-fabrication of graphene-based devices. To address these issues, we combined an array of growth approaches and characterization resources to investigate several innovative and synergistic approaches for the synthesis of high quality graphene films on technologically relevant substrate (SiC and metals). Our work focused on developing the fundamental scientific understanding necessary to generate large-area graphene films that exhibit highly uniform electronic properties and record carrier mobility, as well as developing techniques to transfer graphene onto other substrates.

## ACKNOWLEDGMENTS

The authors would like to thank Tom Zipperian and David Sandison for their visionary leadership in developing the initial stages of this work. The authors would also like to thank the Nanoscience to Microsystems Investment Committee for their support.

### **Team Acknowledgments:**

Stephen W. Howell	Principal Investigator Graphene Transfer Device Fabrication
Carlos Gutierrez	Project Manager
Taisuke Ohta	Graphene Synthesis on SiC LEEM Characterization
Kevin McCarty	Graphene Synthesis on Metals LEEM Characterization
Wei Pan	Low-Temp Magneto Transport
Thomas Beechem	Raman Spectroscopy
Laura Biedermann	Graphene Transfer
Craig Nolen	Graphene Transfer
Anthony Ross	Device Fabrication

# CONTENTS

1. Introduction.....	11
2. Graphene Synthesis on SiC.....	13
2.1 Graphene growth on silicon carbide via thermal decomposition.....	13
2.2 Carbon deposition for growing graphene on silicon carbide .....	16
2.3 Synthesis of bilayer graphene on silicon carbide.....	17
3. Graphene Growth on Metals.....	21
3.1 Underlayer growth mechanism .....	21
3.2 Symmetry mismatch leads to mosaic films on Cu foils.....	22
3.3 Cu(111) can be a superior substrate.....	23
3.4 Au is an excellent substrate.....	24
4. Electrostatic Transfer of Graphene .....	27
4.1 Transfer of epitaxial graphene using an anodic-bonding derived technique .....	27
4.1.1 Experimental considerations .....	28
4.1.2 Optical microscopy and AFM characterization of transferred graphene .....	29
4.1.3 Raman analysis of transferred graphene .....	30
4.1.4 Comparison of transferred graphene’s electronic properties .....	31
4.2 Electrostatic transfer of HOPG to Si <sub>3</sub> N <sub>4</sub> /Si.....	32
5. Fabrication of Graphene Hall Bars and Field Effect Transistors.....	35
5.1 Graphene Hall bar (GHB) fabrication.....	35
5.2 Graphene field effect transistor (GFET) fabrication.....	35
5.3 Characterization of Hall bars and GFETs.....	36
6. Low Temperature Magneto Transport.....	39
6.1 Observation of the integer quantum Hall effect in high quality, uniform wafer-scale epitaxial graphene films.....	39
6.2 Electron-electron interaction in high quality epitaxial graphene .....	43
7. Conclusions.....	49
8. References.....	51
Appendix A: SNL’s Graphene Team Network.....	55
Appendix B: Summary of Major Accomplishments .....	56
Distribution .....	57

## FIGURES

- Figure 1.** A comparison of the morphology of graphene films on Si-terminated SiC(0001) processed under ultrahigh vacuum and argon atmosphere conditions: (a) AFM and LEEM image of graphene on 6H-SiC(0001) with a nominal thickness of 1 ML formed by annealing in UHV at a temperature of about 1280°C; (b) AFM and LEEM image of graphene on 6H-SiC(0001) with a nominal thickness of 1.2 ML formed by annealing in Ar (p=900 mbar, T= 1650°C)..... 14
- Figure 2.** Snapshot AFM and LEEM images of graphene growth on Si-terminated SiC at various annealing temperatures. .... 14
- Figure 3.** The three major growth mechanisms of graphene on Si-terminated SiC growth. For high quality electronic grade large area graphene growth, it is vital to control the appearance of the step-flow growth process and suppress the finger-shaped and arrow-shape growth processes. .... 15
- Figure 4.** Strain and carrier concentration mapping (color online). (a) Mechanical strain-field map, (b) histogram of strain values for (a) categorized by the clusters in Fig. 1(c), (c) electron concentration map, (d) histogram of electron concentrations for (c) categorized by the clusters in Fig. 1(c). Regions of more than 1ML graphene are not shown (blackened out in (a) and (c)). Scan size is  $30 \times 30 \mu\text{m}^2$ . Right bottom: legend for the histogram plots and color-bar scales for strain and carrier concentration. The graphene regions referred to in the histogram legend are strained ML (SML), partially strained ML (PSML), and partially relaxed ML (PRML) ..... 16
- Figure 5.** Raman image (left) acquired via analysis of the 2D mode's peak position that allows for identification of regions of C12 (red) and C13 (blue) along with average Raman spectra of these regions (right). .... 17
- Figure 6.** TOP: The semi-metal (zero bandgap) bandstructure of monolayer graphene; MIDDLE: The zero band gap electronic structure of bilayer graphene in the absence of an applied electric field; BOTTOM: The appearance of a band gap in bilayer graphene as a result of the application of an electric field..... 18
- Figure 7.** Raman, LEED, and AFM characterization of the graphene bilayer sample. (a) Representative spectrum of the bilayer region, with the SiC response removed. The inset shows a 2D band fitted well using four Lorentzian functions, an indication of the graphene bilayer presence. (b) Histogram of the I(D)/I(G) ratio acquired from Raman mapping ( $25 \times 25 \mu\text{m}^2$ , 75 x 75 data points). The inset shows the spatial distribution of the total 2D peak width indicating that the bilayer is present on the terraces (dark regions within inset, total width = $50 \text{ cm}^{-1}$ , whereas thicker graphene layers (bright regions of inset, total width = $70 \text{ cm}^{-1}$ ) are located at atomic steps originating from the SiC. (c) LEED pattern of a bilayer graphene obtained at the illuminating electron energy of 48 eV. (d) AFM topography of the graphene sample. The dashed contour on the plateau indicates the region used for device fabrication. .... 19
- Figure 8.** Underlayer growth mechanism during C deposition. (a,b) Upper panels are LEEM images before and after depositing elemental C at 790 °C. Red dotted line is the boundary between R26 and R0 domains of first-layer graphene. Bright areas are bilayer islands. Lower panels show the cross sections along the black dashed lines before and after growth. (c) Same area at room temperature after growth. The bilayer region inside the orange line was created by a second layer growing from the R26 region across the rotational boundary and into the R0 region. The area inside the green line is a bilayer domain that slowly expanded from a bilayer island present in the R26 domain before C deposition. (d) LEED pattern from the orange area showing

that its topmost layer is R0 graphene. (e) LEED pattern from the green area showing that its topmost layer is R26 graphene..... 21

**Figure 9.** (a) Alignment of graphene on Cu(100). Graphene grows with a wide spread of in-plane orientations centered around two symmetry-equivalent Cu(100) directions. (b) Alignment of graphene on Cu(111). Under optimized conditions, graphene grows closely aligned to a single in-plane orientation. .... 22

**Figure 10.** A graphene lobe (a) on a Cu (001) grain at 790 °C, and the same lobe 820 s later (b). These lobes are outlined in (c) in purple and dark green, respectively. A growth rate that is solely a function of orientation will result in a linear growth trajectory for a point on the crystal edge with a given normal, as shown in (c) for five points defined by normals of 25° (gray), 50° (blue), 115° (green), 140° (red), and 155° (yellow) relative to the slow-growth direction. As the graphene lobe grew, the location of the points on its edge with these normals was tracked in discrete increments (colored dots, solid lines are linear best-fits). The excellent agreement between the data and fits demonstrates the linearity of the growth trajectories for given graphene edge orientations. .... 23

**Figure 11.** Dark-field analysis of graphene grown on Cu(111) at 900 °C. The image is a composite of five dark-field micrographs obtained in 1.5° rotational increments from the Cu[112bar] direction at 0°. The saturation of each color reflects the degree graphene is aligned to each angle. Field of view is 20 μm. .... 24

**Figure 12.** (a) LEEM image of graphene islands, which are bright in the micrograph, on Au(111). Islands nucleate both on terraces and step edges and form a dendritic shape during growth prior to their incorporation into a complete film. (b) Micrograph of the full film. The observed lines are likely wrinkles caused by the difference in thermal expansion between the graphene and Au. (c) Selected area LEED reveals that the graphene orients preferentially in an R0 alignment (shown schematically in (g)), with a small minority of domains rotated by 30 degrees (h). Diffraction from the Au(111) herringbone surface reconstruction is also evident. (d, e, f) A LEEM micrograph sequence of bright-field (d), dark-field of the Au substrate ((e), orange circle in (b)), and dark-field of the R0 orientation ((f), blue circle in (b)) of the same region dramatically demonstrates the dominance of the R0 orientation. Indeed, over 90% of the islands in this region are R0. The field of view for all LEEM micrographs is 9 μm..... 25

**Figure 13.** A diagram of the electrostatic transfer method shows the patterned MLG pressed against the heated acceptor glass substrate. A flat tungsten carbide plate is used as an anode to ensure uniform voltage and pressure. The glass rests on a grounded heated plate (not shown). 28

**Figure 14.** AFM and optical images of MLG transferred to Pyrex. In (a), an AFM scan shows the epitaxial graphene prior to lithography and transfer. In (b), an optical micrograph shows hundreds of 20 x 20 μm<sup>2</sup> squares of transferred graphene on a Pyrex coverslip. (c) An AFM scan of a transferred graphene square on Pyrex. Arrows point to ridges in the transferred graphene. (d) An AFM scan of a strip of transferred graphene surrounded by embossed Pyrex. The arrow points to the tip of the transferred graphene strip. (e, f) Phase (e) and topography (f) AFM scans of a strip of graphene from which the thickness of the transferred graphene was measured, as shown by the profile in (g). Images (a, d–g) are of sample C; images (b) and (c) are of sample A. .... 29

**Figure 15.** Reflection optical micrograph (a), Raman maps (b, c) and average spectra (d) of two squares of multilayer graphene transferred to Pyrex. The correlation with the optical image and the intensity of the 2D mode (b) indicate the consistency of the transfer. The transfer process does not significantly damage the graphene as less than 5% of the graphene, predominately near

the perimeter, displays the disorder-induced D-peak (c, d). Note that all spectra are normalized to the G-peak intensity. In the Raman maps (b) and (c), yellow corresponds to the highest intensity of the analyzed spectral features. .... 31

**Figure 16.** Measured  $R_s$  for several squares of transferred graphene. Insert: optical image of a micro four-probe positioned on a  $20 \times 20 \mu\text{m}^2$  graphene square. .... 31

**Figure 17.** Optical image of Hall bar fabricated from C-face epitaxial graphene. .... 32

**Figure 18.** Various aspects of graphene transfer are outlined via optical microscopy; A) and B) are thin and bulk exfoliated graphite from HOPG bulk transferred to  $\text{Si}_3\text{N}_4$ , C) shows  $10\mu\text{m}$  HOPG pillars, and D), E), F) are patterned HOPG pillars transferred to  $\text{Si}_3\text{N}_4$  substrate. .... 33

**Figure 19.** Reliability of  $200 \text{ nm } \text{Si}_3\text{N}_4$  as an electrostatic target substrate was carried out in A) where little carrier emission is seen up to  $80 \text{ V}$  and in B)  $22 \text{ V}$  was calculated to be the minimum voltage needed to achieve the  $0.4 \text{ MPa}$  HOPG exfoliation pressure. .... 34

**Figure 20.** Optical top down image of graphene Hall bar and cross sectional side view. .... 36

**Figure 21.** Optical top down image of GFET and cross sectional side view. .... 36

**Figure 22.** Typical  $I_d(V_{ds})$  curves for several  $V_g$  levels. .... 37

**Figure 23.**  $I_d(V_g)$  curve for a typical GFET. .... 37

**Figure 24.** Microscopic image of a Hall bar device. Inset shows various devices of different sizes. .... 40

**Figure 25.** (a):  $\rho_{xx}$  and  $\rho_{xy}$  measured in a typical graphene Hall bar device. The sample temperature is  $4 \text{ K}$ . 2(b): Landau fan diagram for Shubnikov-de Haas oscillations. .... 41

**Figure 26.**  $R_s$  measured for multiple devices over three cool-down cycles. .... 42

**Figure 27.** Average  $R_s$  data for eleven devices (excluding device #5) measured in multiple days. .... 42

**Figure 28.** (a) magneto-conductive,  $\Delta\sigma(B) = \sigma_{xx}(B) - \sigma_{xx}(0)$  at three temperatures for sample A. (b) weak-localization fitting to the  $T = 3.6\text{K}$  data. The gray line is the experimental data. The black line is the fitting. .... 44

**Figure 29.**  $I\phi$  versus  $T$  for sample A (squares) and samples B (dots). .... 45

**Figure 30.** Zero B field conductivity versus  $\ln(T)$  for sample A (squares) and sample B (dots). .... 45

**Figure 31.**  $\rho_{xx}$  versus  $B$  for sample B. The insert shows  $\Delta\sigma(B)$  around  $B = 0$ . .... 47

## TABLES

<b>Table 1.</b> Epitaxial graphene samples transferred to Pyrex and Zerodur. ....	30
---	----

## NOMENCLATURE

AFM	atomic force microscopy
FET	field effect transistor
GFET	graphene field effect transistor
HOPG	highly-orientated pyrolytic graphite
IQHE	Integer Quantum Hall Effect
LDRD	laboratory directed research and development
LEEM	low energy electron microscopy
ML	monolayer
MLG	multi-layer graphene
RIE	reactive ion etch
SiC	silicon carbide
SNL	Sandia National Laboratories

# 1. INTRODUCTION

The isolation of graphene monolayers in 2004 has spurred an explosion of international graphene research interest due to its exotic electronic properties. Although intrinsically a high mobility semi-metal ( $\sim 200,000 \text{ cm}^2/\text{Vs}$  when defect-free, versus  $\sim 1500$  for Si and  $\sim 8500$  for GaAs), graphene's physical strength, adaptability to planar processing, micron-scale room temperature ballistic electronic transport behavior, and potential for band gap engineering make it a promising candidate for advancing and possibly replacing silicon technology. All told, graphene offers a rife of possibility for the creation of disruptive high-speed carbon electronic architectures. The promise of graphene has, therefore, attracted considerable interest across the international research community with multiple countries investing 100s of millions to billions of dollars in the development of this material.

Currently, a large amount of research has concentrated on single devices made from randomly placed small graphene domains (often from manually exfoliated highly-oriented pyrolytic graphite – HOPG). To realize graphene's electronic device potential, however, techniques must be developed to reproducibly deposit/synthesize high quality graphene onto technologically-relevant surfaces over large areas. This task, while strategically straightforward, is presently tactically intractable due to a lack of fundamental understanding concerning graphene's formation.

To address this major scientific and technological bottleneck, Sandia National Laboratories (SNL) has funded a three year study to develop differentiating and synergistic approaches that include: (1) developing routes for graphene synthesis on SiC and metal (such as copper) substrates, including necessary understanding of nucleation/growth to achieve large area ( $100 \mu\text{m}^2$ ) domains, (2) developing methods for graphene transfer on relevant surfaces, (3) improving the understanding of intrinsic graphene and relevant defects for nanoelectronics (including the observation of mobilities beyond the presently observed defect-limited  $\sim 10,000 \text{ cm}^2/\text{Vs}$  towards the suggested  $\sim 200,000 \text{ cm}^2/\text{Vs}$  limit from exfoliated samples).

The following sections will discuss the various accomplishments that were achieved during this three-year project: (1) development of a scalable synthesis route for mono/bilayer graphene on SiC using atmospheric Ar, (2) development of a fundamental scientific understanding of growth mechanisms for graphene on SiC and metal substrates, (3) the development of a scalable electrostatic graphene transfer process, (4) demonstration of graphene-base field effect transistors, and (5) observation of the Integer Quantum Hall Effect (IQHE) and a record carrier mobility of  $14,000 \text{ cm}^2/\text{Vs}$  for arrays of devices.



## 2. GRAPHENE SYNTHESIS ON SiC

### 2.1 Graphene growth on silicon carbide via thermal decomposition

To realize graphene-based electronics adaptable to standard semiconductor processing capabilities, the development of a wafer-scale production of electronic-grade single crystal graphene films is essential. Since a reliable wafer scale graphene synthesis capability depends on an adequate scientific understanding of graphene nucleation and growth, this project had a major focus towards the basic science understanding of large scale graphene synthesis on silicon-carbide substrates (SiC). The understanding of the growth of epitaxial graphene on SiC was seen as an excellent test system yielding key scientific understanding that would be translatable to other systems (i.e., graphene on copper). Upon the project's initiation, it was known that a few-layer thick epitaxial graphene films could be readily grown on SiC(0001) substrate (Si-termination) by high temperature decomposition of SiC in a synthesis approach generally termed as graphitization [1]. At elevated temperature, Si atoms preferentially sublime from a SiC substrate, leaving behind carbon atoms at the surface that crystallize into graphene films. However, critical scientific understanding was lacking for this process. For instance, the detailed atomistic processes of this graphitization synthesis approach, in particular the diffusion of surface carbon atoms, were not understood. Nonetheless, there was significant interest in graphene-based nanoelectronics fabricated on silicon carbide [2].

To this end, our research effort first focused on developing a differentiating capability at Sandia for growing large-area epitaxial graphene films on SiC using an atmospheric-pressure high-temperature furnace, a newly reported synthesis approach [3]. It was hypothesized that the argon (Ar) atmosphere used in the process slows down the sublimation of Si at elevated temperatures, thus enabling improved control of Si sublimation and carbon diffusion at higher processing temperatures, and consequently promoting the higher quality graphene growth (see Figure 1). This effort was initially conducted in collaboration between Ronald Loehman and the Advanced Materials Laboratory (AML), and later transferred to the Integrated Materials Research Laboratory (IMRL). The characterization of the graphene films were carried out using low energy electron microscopy (LEEM), atomic force microscopy (AFM), and Raman spectroscopy. Raman spectroscopy measurements took place using a WITec Raman imaging system with 532 nm incident laser light. We have shown the successful synthesis capability of large-area graphene monolayer films, which were then used in various activities in this program described in the other sections of this SAND report.

Our work investigated the relationship between annealing and hydrogen pre-annealing processing temperatures, as well as annealing ramp rate on graphene morphology (Figure 2). To gain further fundamental understanding of the Ar-atmosphere graphene growth and to further improve the quality of the films, we investigated the atomic structure, morphology, and the growth process of partially graphene grown films in collaboration with Norman Bartelt, Shu Nie, Konrad Thürmer from Materials Physics Department, and Gary Kellogg from Surface and Interface Sciences Department at Sandia National Laboratories. We found that the first layer of graphene growth involves three different growth mechanisms, and that the diffusion of carbon atoms and the atomic step structures of a starting SiC morphology dictate which mechanism governs the growth in microscopic scale. The result was published in reference [4]. Based on

this new scientific understanding, we further improved the reproducibility of the graphene films quality by tailoring the step structure of SiC substrate. Figure 3 shows the desired step-flow growth, as well as arrow-growth and finger-growth.

The three different growth mechanisms prompted us to study a mechanical property of monolayer epitaxial graphene using Raman spectroscopy and microscopy. Raman spectroscopy is a direct probe of the phonon frequency in materials that is sensitive to their strain and electronic dispersion. Using this method, we found a significant lateral strain variation within the monolithic graphene monolayer and the coupling between the exerted strain and the concentration of charge carriers, which is one of the fundamental relationships in material physics. This work is carried out in collaboration with Diedrich Schmidt at Ruhr-University Bochum. The publication generated from this work is currently under review [5] (See Figure 4).

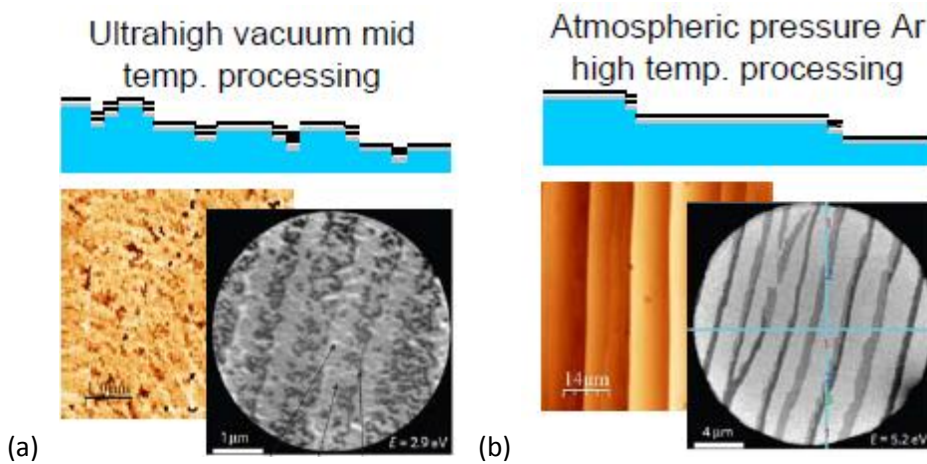


**Figure 1.** A comparison of the morphology of graphene films on Si-terminated SiC(0001) processed under ultrahigh vacuum and argon atmosphere conditions: (a) AFM and LEEM image of graphene on 6H-SiC(0001) with a nominal thickness of 1 ML formed by annealing in UHV at a temperature of about 1280°C; (b) AFM and LEEM image of graphene on 6H-SiC(0001) with a nominal thickness of 1.2 ML formed by annealing in Ar ( $p=900$  mbar,  $T= 1650^{\circ}\text{C}$ ).

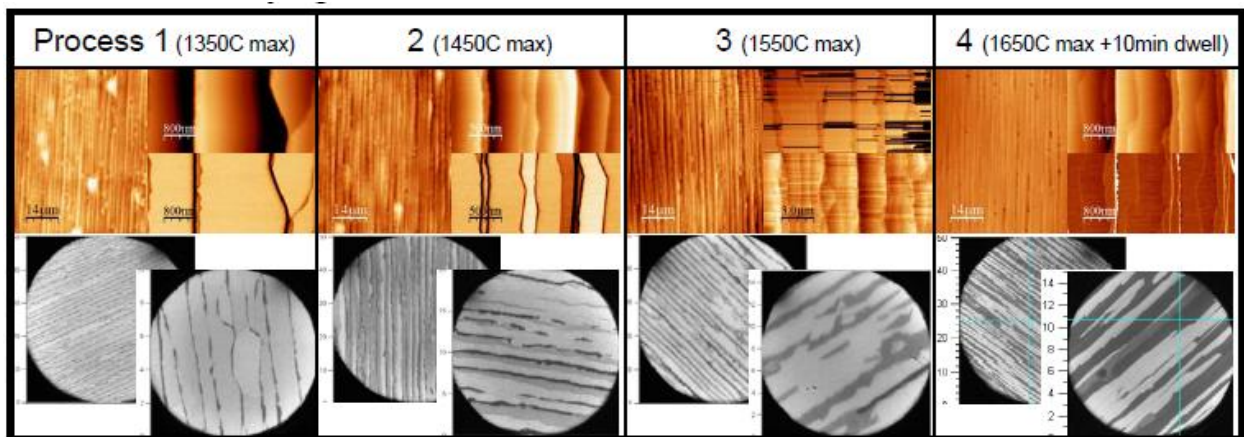


**Figure 2.** Snapshot AFM and LEEM images of graphene growth on Si-terminated SiC at various annealing temperatures.

# Morphology of buffer layer surface

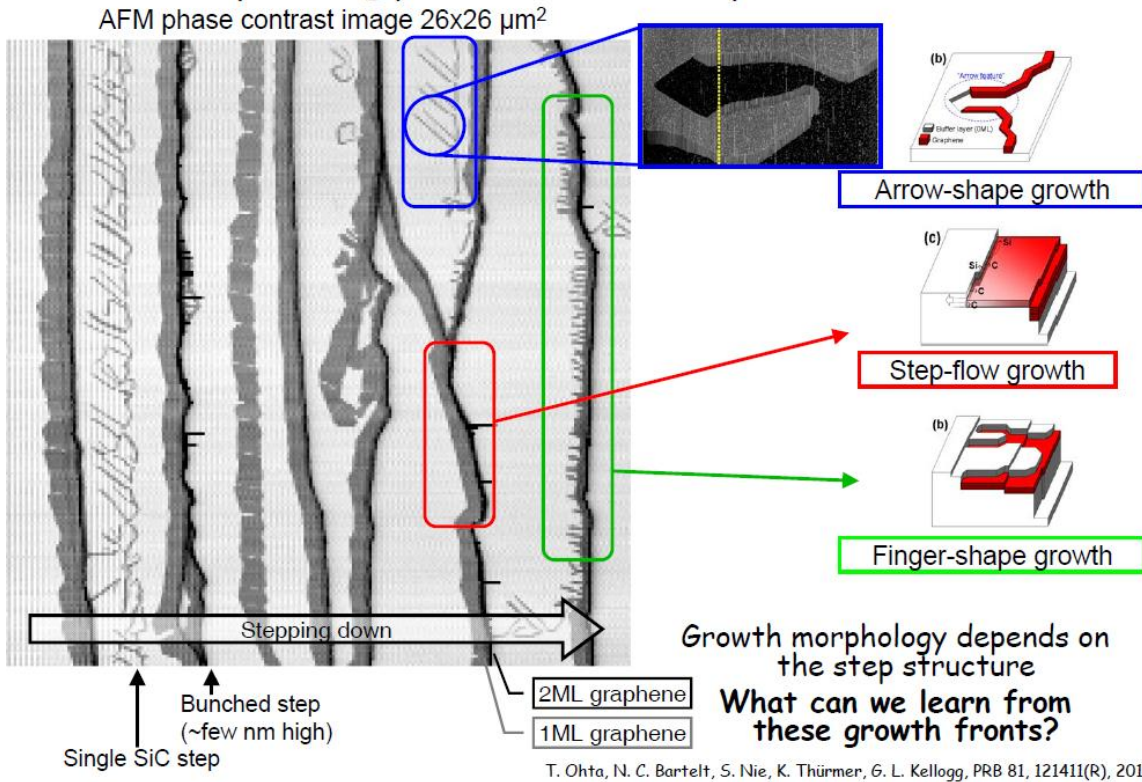


**Figure 3.** The three major growth mechanisms of graphene on Si-terminated SiC growth. For high quality electronic grade large area graphene growth, it is vital to control the appearance of the step-flow growth process and suppress the finger-shaped and arrow-shape growth processes.

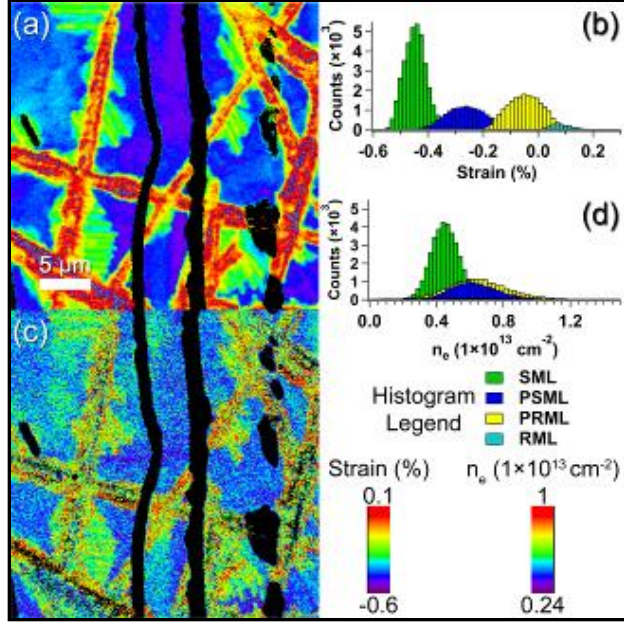


**Figure 4.** Strain and carrier concentration mapping (color online). (a) Mechanical strain-field map, (b) histogram of strain values for (a) categorized by the clusters in Fig. 1(c), (c) electron concentration map, (d) histogram of electron concentrations for (c) categorized by the clusters in Fig. 1(c). Regions of more than 1ML graphene are not shown (blackened out in (a) and (c)). Scan size is  $30 \times 30 \mu\text{m}^2$ . Right bottom: legend for the histogram plots and color-bar scales for strain and carrier concentration. The graphene regions referred to in the histogram legend are strained ML (SML), partially strained ML (PSML), and partially relaxed ML (PRML)

## 2.2 Carbon deposition for growing graphene on silicon carbide

A rational extension of the graphene growth on SiC is the use of a carbon source to promote thin film deposition process for a more predictable graphene synthesis. Toward this goal, we have carried out in-situ observations of graphene growth by carbon deposition in LEEM using a solid graphite and an isotopically enriched  $^{13}\text{C}$  graphite sources. The isotope labeling also provides us a fundamental understanding of the graphene-substrate interface structure using Raman spectroscopy (Figure 5). We have completed the experiments, and are currently analyzing the result. Our preliminary analysis alludes to the mixing of deposited carbon atoms with the substrate carbons, suggesting the crucial role of the interface structure. We anticipate this result be published in the near future.

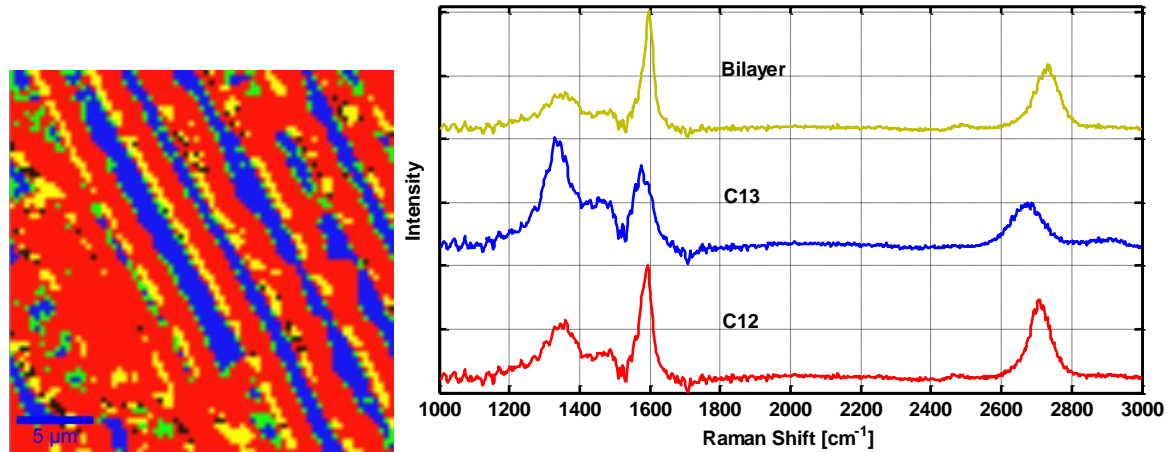


**Figure 5.** Raman image (left) acquired via analysis of the 2D mode's peak position that allows for identification of regions of C12 (red) and C13 (blue) along with average Raman spectra of these regions (right).

### 2.3 Synthesis of bilayer graphene on silicon carbide

One of the most pressing issues in the current graphene research is the creation and the control of the electronic band gap to exploit this material in digital electronics. Graphene nanoribbons (GNR) have been viewed as one possible approach for inducing a band gap in graphene, but at present the processing challenges for reliably producing GNRs for devices is a serious obstacle. Bilayer graphene with Bernal stacking structure avoids many of the processing challenges presented by GNRs, and is regarded as one of the more viable approaches towards inducing and tuning a band gap in graphene by the application of a transverse electric field perpendicular to the two stacked graphene monolayers (Figure 6). However, the growth of large-area bilayer graphene films, in particular the control of their stacking, turned out to be a challenging issue, only reported on SiC substrate and verified from its electronic dispersion. Its full verification in terms of the electronic transport properties has not been reported.

We have taken on this challenge via synthesizing quasi-free standing bilayer graphene on SiC. It was recently reported that hydrogen can be inserted between epitaxial graphene and SiC substrate, practically decoupling graphene layers from the substrate [6]. In collaboration with Emanuel Tutuc at University of Texas at Austin, we have shown that quasi-free standing bilayer graphene on SiC indeed exhibits the signature of Bernal stacking from its quantum Hall states (Figure 7). This is the first demonstration that bilayer graphene grown on SiC is a viable material for realizing graphene-based digital electronics. The result was published in Ref. [7].

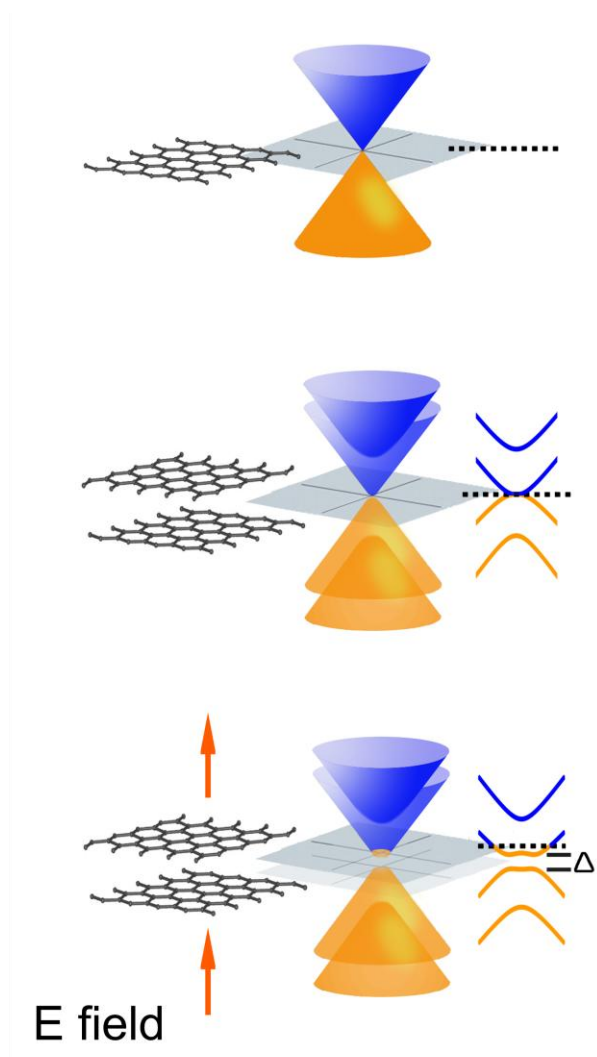


**Figure 6.** TOP: The semi-metal (zero bandgap) bandstructure of monolayer graphene; MIDDLE: The zero band gap electronic structure of bilayer graphene in the absence of an applied electric field; BOTTOM: The appearance of a band gap in bilayer graphene as a result of the application of an electric field.

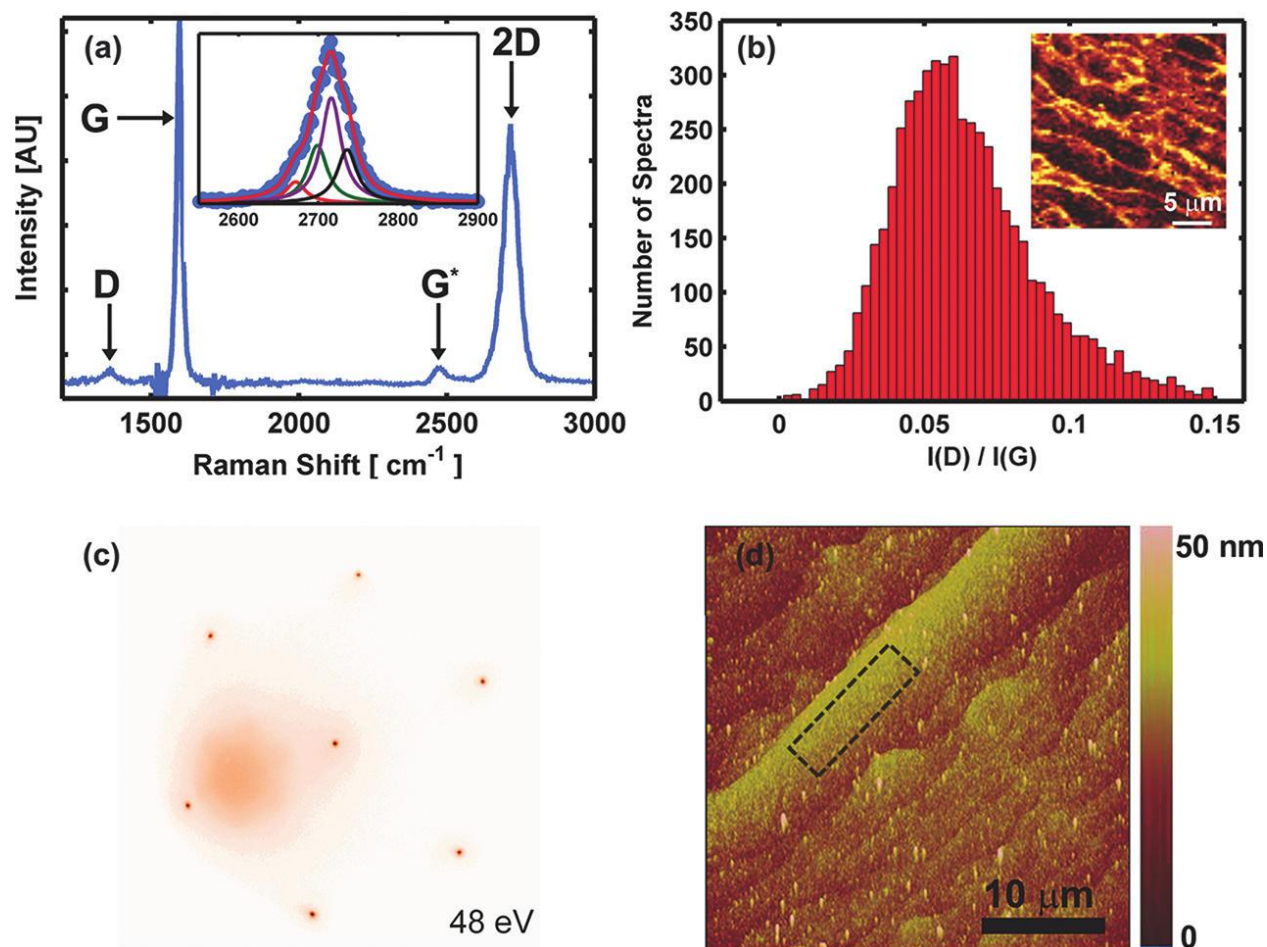


**Figure 7.** Raman, LEED, and AFM characterization of the graphene bilayer sample. (a) Representative spectrum of the bilayer region, with the SiC response removed. The inset shows a 2D band fitted well using four Lorentzian functions, an indication of the graphene bilayer presence. (b) Histogram of the  $I(D)/I(G)$  ratio acquired from Raman mapping ( $25 \times 25 \mu\text{m}^2$ ,  $75 \times 75$  data points). The inset shows the spatial distribution of the total 2D peak width indicating that the bilayer is present on the terraces (dark regions within inset, total width  $=50 \text{ cm}^{-1}$ ), whereas thicker graphene layers (bright regions of inset, total width  $=70 \text{ cm}^{-1}$ ) are located at atomic steps originating from the SiC. (c) LEED pattern of a bilayer graphene obtained at the illuminating electron energy of 48 eV. (d) AFM topography of the graphene sample. The dashed contour on the plateau indicates the region used for device fabrication.



### 3. GRAPHENE GROWTH ON METALS

Growth on transition-metal substrates has emerged as a leading approach to synthesize graphene films of high quality and large area. For application, the films are typically transferred to another substrate, such as silicon, usually by first dissolving the metal. In this LDRD, we used low-energy electron microscopy (LEEM) to observe graphene growing on four different metals: Ir, Pd, Cu and Au. We determined the relationships between the growth mechanism and the film properties. This information provides direct insight into how to improve the film quality by manipulating the growth methods.

#### 3.1 Underlayer growth mechanism

Growth on metals with low C solubility like Cu self-limit to one graphene layer in CVD processes. This is an advantage for applications requiring monolayer films but a disadvantage for producing bilayers. So the question is how do bilayers form on metals? The consensus in the literature has been that the second and subsequent layers grow as in conventional crystal growth, that is, on top of prior layers. But our results show that this is not the case – we have established conclusively that the second layer grows between the first layer and the substrate no matter what the source of C. That is both C segregating from the substrate and C deposited on top of the first layer lead to “interlayer” growth. We established the growth mechanism studying growth on Ir(111) where the occurrence of domains with different in-plane orientations allows determining where the second layer grows [8,9]. In the method, the in-plane orientation of the first graphene layer in a region is mapped. This same region was characterized after the second layer was grown. Low-energy electron diffraction (LEED) established that the second layer grew next to the substrate, not on top of the first layer, even when the C was deposited from above (Figure 8).

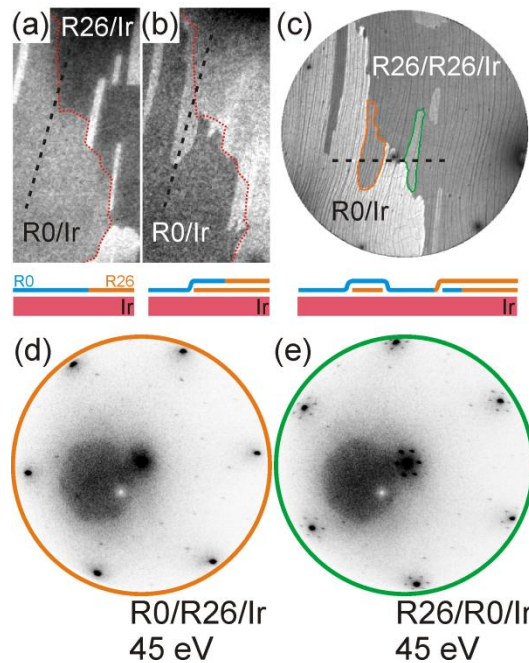


**Figure 8.** Underlayer growth mechanism during C deposition. (a,b) Upper panels are LEEM images before and after depositing elemental C at 790 °C. Red dotted line is the boundary between R26 and R0 domains of first-layer graphene. Bright areas are bilayer islands. Lower panels show the cross sections

along the black dashed lines before and after growth. (c) Same area at room temperature after growth. The bilayer region inside the orange line was created by a second layer growing from the R26 region across the rotational boundary and into the R0 region. The area inside the green line is a bilayer domain that slowly expanded from a bilayer island present in the R26 domain before C deposition. (d) LEED pattern from the orange area showing that its topmost layer is R0 graphene. (e) LEED pattern from the green area showing that its topmost layer is R26 graphene.

The “underlayer” mechanism has important implications for multilayer growth on metals. Namely metals that weakly bind to the graphene are unstable towards making multilayer mounds rather than uniformly thick layers. In fact, we observe mound formation on Ir [8] and Pd(111) [10]. In contrast, uniform films can be grown on substrates that strongly bind to graphene. Consistently, we observe uniform film formation on Ru(0001).

### 3.2 Symmetry mismatch leads to mosaic films on Cu foils

A breakthrough in large-area graphene synthesis occurred by using low-cost Cu foils. Our work gave new insight into the growth mechanism and limitations of the foil approach. We first determined that the commercial Cu foils had pronounced (100) crystallographic texture, a result of cold rolling followed by recrystallization at growth temperatures. Then we discovered that graphene on Cu(001) has large rotational disorder. One source of the disorder is the inherent result of symmetry – the 6-fold graphene forms around two crystallographically equivalent orientations on the 4-fold substrate [11]. Even worse, substantial disorder occurs around these two in-plane orientations, with the graphene being rotationally smeared over  $\pm 7^\circ$  (Figure 9). The in-situ observations also revealed that graphene grows as loped islands on Cu(001) (Figure 10), a consequence of attachment-limited growth kinetics.

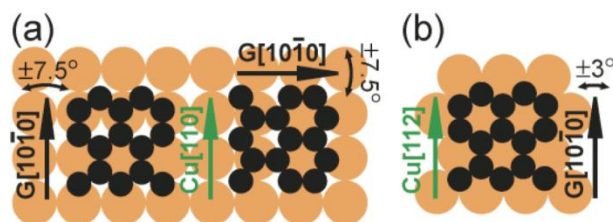


**Figure 9.** (a) Alignment of graphene on Cu(100). Graphene grows with a wide spread of in-plane orientations centered around two symmetry-equivalent Cu(100) directions. (b) Alignment of graphene on Cu(111). Under optimized conditions, graphene grows closely aligned to a single in-plane orientation.

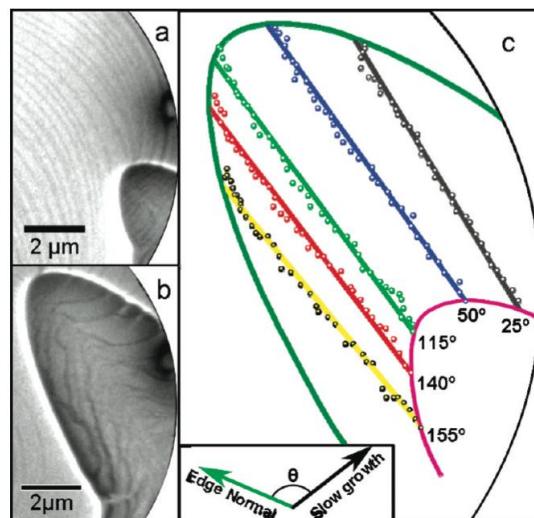


**Figure 10.** A graphene lobe (a) on a Cu (001) grain at 790 °C, and the same lobe 820 s later (b). These lobes are outlined in (c) in purple and dark green, respectively. A growth rate that is solely a function of orientation will result in a linear growth trajectory for a point on the crystal edge with a given normal, as shown in (c) for five points defined by normals of 25° (gray), 50° (blue), 115° (green), 140° (red), and 155° (yellow) relative to the slow-growth direction. As the graphene lobe grew, the location of the points on its edge with these normals was tracked in discrete increments (colored dots, solid lines are linear best-fits). The excellent agreement between the data and fits demonstrates the linearity of the growth trajectories for given graphene edge orientations.

### 3.3 Cu(111) can be a superior substrate

The (001) texture of the commonly used Cu foils result from their production method (rolling). But foils or large-area films of (111) textured Cu are easily achieved because the (111) surface has lower surface energy than (001). We found that Cu(111) had distinct advantages as a substrate. We determined that graphene quality on Cu(111) was a strong function of the substrate morphology – bunches of substrate steps lead to rotational disorder. In fact, we directly observed that step bunches can cause a graphene sheet to change orientation as the bunches are overgrown. However, using clean and smooth Cu(111) we were able to produce graphene islands well aligned to a single in-plane direction ( Figure 11). This result shows that Cu(111) offers an approach to synthesize graphene films with only small angle boundaries between the separately nucleated domains [12]. Finally, we found that growth on Cu(111) was a diffusion-limited process, in marked contrast to Cu(001), Ir(111) and Ru(0001).

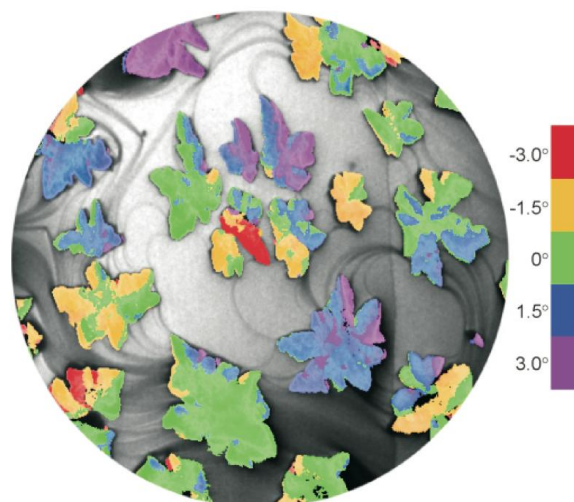


**Figure 11.** Dark-field analysis of graphene grown on Cu(111) at 900 °C. The image is a composite of five dark-field micrographs obtained in 1.5° rotational increments from the Cu[112bar] direction at 0°. The saturation of each color reflects the degree graphene is aligned to each angle. Field of view is 20 μm.

### 3.4 Au is an excellent substrate

Au is almost unexplored as a substrate for graphene growth even though proven methods exist to make large-area Au films and foils, electrochemically dissolve Au and recycle the material back into substrate form. The principle reason for the lack of attention is that Au's low catalytic activity precludes simple CVD processing. We overcame this challenge by growing graphene on Au(111) by depositing evaporated C, which is a manufacturable process. We found that we could synthesize graphene in which about 95% of the domains were closely aligned to a single in-plane orientation (Figure 12) [13]. Complete films were achieved through the C deposition approach. Angle-resolved photoemission performed in collaboration with Lawrence Berkeley National Laboratory (LBNL) revealed that the films on the Au had the almost the same perfect linear electronic dispersion found in free-standing graphene. So Au is a viable substrate for graphene growth.

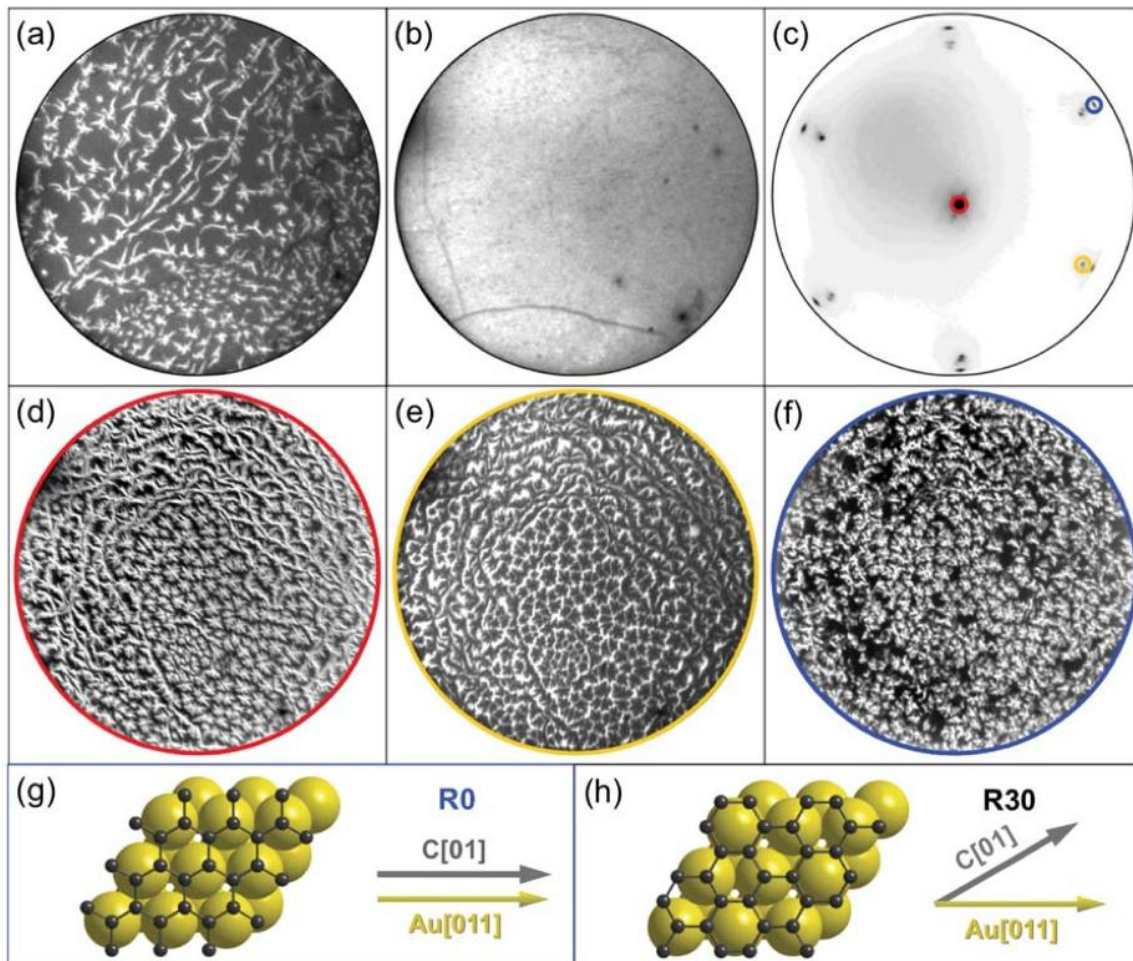


**Figure 12.** (a) LEEM image of graphene islands, which are bright in the micrograph, on Au(111). Islands nucleate both on terraces and step edges and form a dendritic shape during growth prior to their incorporation into a complete film. (b) Micrograph of the full film. The observed lines are likely wrinkles caused by the difference in thermal expansion between the graphene and Au. (c) Selected area LEED reveals that the graphene orients preferentially in an R0 alignment (shown schematically in (g)), with a small minority of domains rotated by 30 degrees (h). Diffraction from the Au(111) herringbone surface reconstruction is also evident. (d, e, f) A LEEM micrograph sequence of bright-field (d), dark-field of the Au substrate ((e), orange circle in (b)), and dark-field of the R0 orientation ((f), blue circle in (b)) of the same region dramatically demonstrates the dominance of the R0 orientation. Indeed, over 90% of the islands in this region are R0. The field of view for all LEEM micrographs is 9  $\mu\text{m}$ .



## 4. ELECTROSTATIC TRANSFER OF GRAPHENE

### 4.1 Transfer of epitaxial graphene using an anodic-bonding derived technique

Graphene due to its phenomenal electrical, thermal, and mechanical properties, is an eminently suitable material for diverse applications such as frequency multipliers, high-speed transistors, gas sensors, and transparent conductive electrodes [14,15]. As these applications require graphene on a variety of substrates, readily transferrable graphene grown via chemical vapor deposition (CVD) on Ni [16] or Cu [11] is frequently used. CVD-graphene from Cu or Ni is not ideal as it has lower mobilities, smaller domain sizes than epitaxial graphene [11], and may be contaminated with the Cu/Ni substrate elements.

Techniques to transfer epitaxial graphene to arbitrary substrates include mechanical exfoliation using tape [17,18] and peeling the graphene layers using a metal/polyimide film [19]. Electrostatic transfer, an anodic bonding-derived technique, offers an alternative method for transferring epitaxial graphene. Random graphite flakes have been electrostatically deposited from HOPG onto Pyrex and silicon wafers [20-22].

This electrostatic transfer process relies on the presence of mobile alkali cations in the glass to induce the transfer of graphene, similar to traditional anodic bonding. In anodic bonding, these cations, under the presence of a large applied potential, serve to enhance the electric field at the interface between the metal (anode) and glass (cathode). A key distinction between electrostatic deposition of graphite and anodic bonding is that the graphite is transferred to the glass, not covalently bonded.

An estimate for the electric field generated during anodic bonding of metal to Pyrex was experimentally estimated by Wallis and Pomerantz, who estimated 300 MV/m for an 800 V applied voltage [23]. Furthermore, this interface can be modeled as a pair of parallel conductor plates, from which the electrostatic pressure can be calculated. The minimum stress to exfoliate a graphene monolayer from bulk graphite is  $P = 0.4 \text{ MPa}$  [22]. The pressure between the graphene and glass is estimated at  $P = \frac{1}{2}\epsilon_0\epsilon_r E^2$ , where  $\epsilon_0$  is the permittivity of free space,  $\epsilon_r$  is the dielectric constant of the glass (4.6 for Pyrex at room temperature), and assuming  $E = 300 \text{ MV/m}$ . The electrostatic pressure at a metal/Pyrex interface is  $\sim 2 \text{ MPa}$ , sufficient to exfoliate a graphene monolayer.

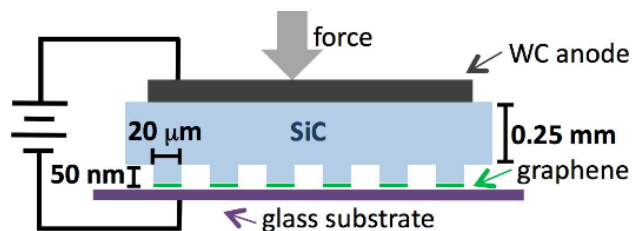


**Figure 13.** A diagram of the electrostatic transfer method shows the patterned MLG pressed against the heated acceptor glass substrate. A flat tungsten carbide plate is used as an anode to ensure uniform voltage and pressure. The glass rests on a grounded heated plate (not shown).

The following describes an electrostatic technique for transferring patterned multilayer epitaxial graphene (MLG) to insulating glass substrates, as indicated in Figure 13. The acceptor substrates used were Pyrex and Zerodur. With this method, we have transferred thousands of pre-patterned MEG squares to the acceptor glass substrates. Electrostatic transfer offers a scalable process enabling wafer-level production of graphene devices [24].

#### 4.1.1 Experimental considerations

*Epitaxial Graphene Synthesis and Lithography:* MLG was grown on n-type 6H-SiC(000-1) (C-face, 0.069  $\Omega$ -cm, Cree Inc.) using an Ar-mediated growth process [4]. The as-grown graphene samples were defined by smooth graphene domains bounded by ridges with heights 5–80 nm tall and widths 100–750 nm wide. An atomic force microscope (AFM) scan of a typical region is shown in Figure 14(a). The graphene drapes continuously over the underlying SiC terraces, highlighted by dashed lines, which are a few microns wide and 5–10 nm high.

Optical lithography and reactive ion etching were used to define patterned graphene regions, typically pillars 50 nm tall and  $20 \times 20 \mu\text{m}^2$  across. Post-lithography Raman analysis showed that the graphene was undamaged, except at the perimeter of the graphene regions, and that the photoresist was removed.

*Electrostatic Transfer of Graphene:* Electrostatic transfer of graphene to Pyrex microscope slides and coverslips and a Zerodur optical flat was carried out using a custom anodic bonder. Prior to transfer, the slides were cleaned by soaking in piranha, rinsing with DI water, and drying with compressed air.

**Figure 13 shows a diagram of the electrostatic transfer procedure. First a force of 2–10 N is applied to press the patterned MLG into intimate contact with the glass substrate.**

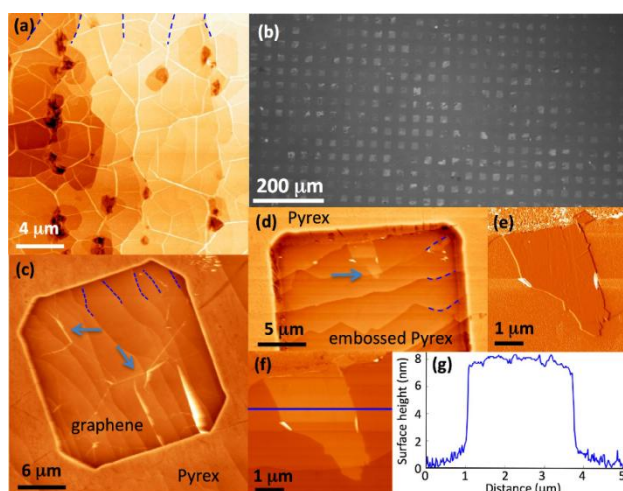
**The sample stack is then heated to 300 °C under pressure. When the set point temperature is reached, the potential voltage is gradually increased to the transfer voltage, 1.2 kV. At the transfer voltage, a rapidly decaying current flows. This voltage is maintained until the measured current drops from ~0.3 mA to below 0.02 mA, a time of 5–15 minutes. Subsequently, the sample stack is cooled to room temperature, and the samples are separated.**

Table 1 lists the graphene samples transferred to glass; samples A, C, and D will be discussed in more detail [24].

#### 4.1.2 Optical microscopy and AFM characterization of transferred graphene

We have electrostatically transferred large areas ( $\sim 10 \text{ mm}^2$ ) of patterned MLG to multiply substrates. An optical micrograph of a  $\sim 1.0 \times 0.5 \text{ mm}^2$  area of transferred graphene (sample A) on Pyrex is shown in Figure 14(b). The variation in optical intensity of the graphene is attributed to the variation in thickness of the transferred graphene. In the case of perfect transfer, graphene would cover 25% of the Pyrex substrate. In the optical image in Figure 14(b), graphene covers  $12 \pm 2\%$  of the Pyrex, a transfer efficiency of  $\sim 50\%$ . The transfer efficiencies for all samples are listed in

Table 1.



**Figure 14.** AFM and optical images of MLG transferred to Pyrex. In (a), an AFM scan shows the epitaxial graphene prior to lithography and transfer. In (b), an optical micrograph shows hundreds of  $20 \times 20 \mu\text{m}^2$  squares of transferred graphene on a Pyrex coverslip. (c) An AFM scan of a transferred graphene square on Pyrex. Arrows point to ridges in the transferred graphene. (d) An AFM scan of a strip of transferred graphene surrounded by embossed Pyrex. The arrow points to the tip of the transferred graphene strip. (e, f) Phase (e) and topography (f) AFM scans of a strip of graphene from which the thickness of the transferred graphene was measured, as shown by the profile in (g). Images (a, d–g) are of sample C; images (b) and (c) are of sample A.

Figure 14(c) shows an AFM scan of a transferred graphene square on a Pyrex coverslip. Full-square transfer to Pyrex was confirmed using optical microscopy and phase contrast AFM (not shown). The morphology of the transferred graphene resembles that of epitaxial graphene; however, in the transferred graphene, the ridge height (5–20 nm) and density are less than in the donor MEG.

The thickness of the transferred graphene is estimated by AFM height measurements of a torn piece of a graphene square. Figure 14(d) shows an AFM topography image of a strip of transferred graphene (indicated by the blue arrow), which drapes over an embossed step edge feature. A slight phase contrast between the graphene strip and the embossed Pyrex region is seen in Figure 14(e). Histogram measurements of the height of the graphene strip in Figure 14(f)

and the profile in Figure 14(g), show that the height of the transferred graphene is  $5.9 \pm 0.2$  nm, corresponding to  $\sim 18$  layers of graphene [24].

**Table 1.** Epitaxial graphene samples transferred to Pyrex and Zerodur.

Sample	Growth temp (°C)	Anneal time (min)	Acceptor substrate	Pattern size ( $\mu\text{m} \times \mu\text{m}$ )	Transfer efficiency (%)
A	1700	5	Pyrex coverslip	20 x 20	$63 \pm 7^a$
B	1650	30	Pyrex slide	20 x 20	$57 \pm 3^a$
C	1650	10	Pyrex slide	20 x 20	$43 \pm 2^a$
D	1650	10	Zerodur	70 x 70	$93 \pm 5^b$

<sup>a</sup>Where 100 % efficiency corresponds to graphene squares covering 25 % of the acceptor substrate over a  $0.37 \text{ mm}^2$  region.

<sup>b</sup>Where 100% efficiency corresponds to a  $70 \times 70 \mu\text{m}^2$  region entirely covered by graphene.

#### 4.1.3 Raman analysis of transferred graphene

To confirm the transfer of epitaxial graphene to the Pyrex substrate and to evaluate their quality, Raman images of the samples were acquired before and after the electrostatic transfer. Raman maps and spectra were obtained using a WITec alpha 300 R confocal Raman microscope with a 523 nm laser. Images were collected from a series of spectra spaced at  $360\text{-nm}$  across regions of the sample spanning at least  $1125 \mu\text{m}^2$ . The presence and uniformity of the transferred graphene were investigated by examining the intensity, peak position, and FWHM of graphene's D, G, and 2D (G') Raman active modes at  $\sim 1350 \text{ cm}^{-1}$ ,  $\sim 1580 \text{ cm}^{-1}$ , and  $\sim 2700 \text{ cm}^{-1}$ , respectively [25,26].

An optical micrograph and Raman image of the 2D mode intensity, Figure 15 (a) and (b), respectively, confirm that MLG was consistently transferred to a Pyrex slide (sample C). Thicker graphene is indicated by greater 2D mode intensity in Figure 15(b). The D peak is observed only within  $\sim 1\mu\text{m}$  of the perimeter of the transferred graphene, indicating that the electrostatic transfer does not damage the graphene (Figure 15(c)). Such perimeter damage was also observed in Raman maps (not shown) of the epitaxial graphene pillars on SiC prior to transfer, indicating that the lithography process slightly damages the graphene perimeter. Furthermore, only the graphene is transferred as no spectral features from the SiC are observed in the representative spectra shown in Figure 15 (d).

Analysis of Raman spectra peak positions suggests that the transfer process only marginally modifies the graphene. The G-peak position of the transferred MLG is downshifted by  $4 \text{ cm}^{-1}$ , as compared to the original epitaxial graphene. The G-peak position is sensitive to both substrate charges and strain. As the transferred graphene samples are thick (e.g.  $\sim 18$  ML flake in Figure 14(f)), substrate charges are screened and thus will not affect the G-peak position of the samples [27,28]. Therefore, the downshift is induced by the application of a small tensile strain that arises due to the transfer process [24].

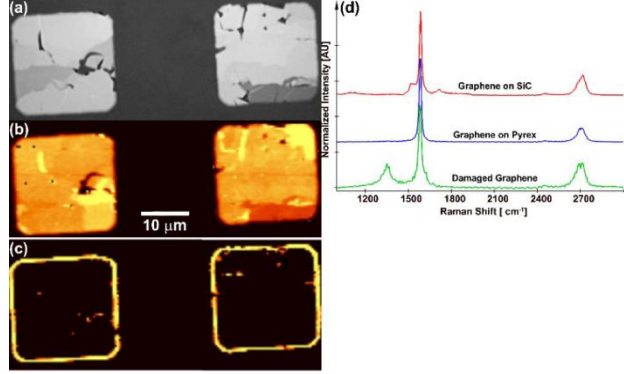


**Figure 15.** Reflection optical micrograph (a), Raman maps (b, c) and average spectra (d) of two squares of multilayer graphene transferred to Pyrex. The correlation with the optical image and the intensity of the 2D mode (b) indicate the consistency of the transfer. The transfer process does not significantly damage the graphene as less than 5% of the graphene, predominately near the perimeter, displays the disorder-induced D-peak (c, d). Note that all spectra are normalized to the G-peak intensity. In the Raman maps (b) and (c), yellow corresponds to the highest intensity of the analyzed spectral features.

#### 4.1.4 Comparison of transferred graphene's electronic properties

To gauge the impact of electrostatic transfer on graphene's electronic properties, sheet resistance ( $R_s$ ) of graphene transferred to Pyrex and Zerodur was compared to the  $R_s$  of epitaxial graphene grown on the carbon face of SiC. To measure the  $R_s$  of transferred graphene (samples A and D) a linear micro four-probe was used. This four-probe was comprised of four  $3\mu\text{m}$  wide cantilevers with a  $5\mu\text{m}$  pitch. The insert in Figure 16 shows an optical image of the four-probe positioned on a  $20 \times 20\mu\text{m}^2$  square of transferred graphene. Since the thickness of graphene is much less than the probes spacing,  $R_s$  can be calculated from

$$R_s = \frac{\pi}{\ln 2} \frac{\Delta V}{I},$$

where  $\Delta V$  is the voltage drop measured between the inner two probes and  $I$  is the current sourced through the outer two probes. The average  $R_s$  of three transferred graphene squares on Pyrex was found to be  $320 \pm 50\ \Omega/\square$  (excluding a large outlier), where the individual  $R_s$  values were 150, 180, 250, and  $705\ \Omega/\square$ ; for graphene on Zerodur, the average  $R_s$  was  $250 \pm 90\ \Omega/\square$ , where the individual values were 150, 260, and  $330\ \Omega/\square$ . Figure 4 summarizes the  $R_s$  data. The high variance in  $R_s$  is attributed to the variation in thickness of the transferred graphene films.

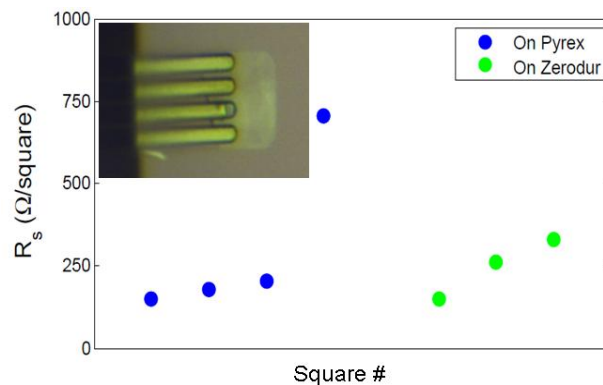


**Figure 16.** Measured  $R_s$  for several squares of transferred graphene. Insert: optical image of a micro four-probe positioned on a  $20 \times 20\mu\text{m}^2$  graphene square.

In addition to probing the sheet resistance of transferred graphene, several Hall bar structures were fabricated from epitaxial graphene grown on the carbon face of SiC. Since this graphitic material is similar to the material used for the transfer, it served as a gauge to determine how the transfer process affects the graphene. Figure 17 shows an optical image of a typical Hall bar that was fabricated using standard optical lithography [29]. The average  $R_s$  was found to be  $180 \pm 70 \Omega/\square$  at a temperature of 10K (low temperature was required to freeze out carriers present in the highly doped SiC substrate). Comparison of  $R_s$  for transferred and epitaxial graphene show similar values, indicating very little modification in  $R_s$  due to the transfer process. Direct comparisons of sheet resistance are problematic since the thickness of graphene varies. For thermal tape transferred carbon face epitaxial graphene on SiO<sub>2</sub>, Caldwell et al. reported  $R_s = 175 \Omega/\square$  [18]. For an additional comparison, using the same four-probe procedure, we measured  $R_s = 3.3 \pm 1.1 \Omega/\square$  for HOPG (SPI-1 grade).

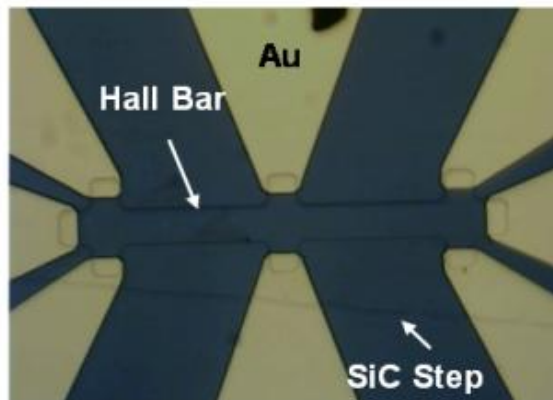


**Figure 17.** Optical image of Hall bar fabricated from C-face epitaxial graphene.

## 4.2 Electrostatic transfer of HOPG to Si<sub>3</sub>N<sub>4</sub>/Si

Recent advancements in controlled high-quality uniform layer growth of graphene through chemical vapor deposition (CVD) on Cu [30] or growth by thermal decomposition on SiC (0001) [4] over wafer-sized areas has been the current focus of graphene research. Through these developments, the motivation for transferring graphene from its growth medium (usually a metal [16]) to arbitrary dielectrics of choice has rapidly grown in importance. This is in part due to corporate and governmental motivations to seek out the commercial and industrial viability for securing graphene as a material with parallel fabrication capability. Severe limitations exist for transferring large-areas of graphene including processes which chemically degrade graphene or leave residues [31], are not suitable for parallel fabrication [32], are only good for few specific applications [33], can only be used for HOPG bulk transfer [21], etc.

Work completed at SNL has been to research and develop an electrostatic graphene transfer process. Our goal is to produce a reliable high-quality wafer-scale transfer apparatus that is compatible with future parallel graphene fabrication processes. Our results prove that we have now matched the results of current electrostatic transferring processes [21,24,34] of transferring HOPG pillars, defined using photolithographic patterning, to common dielectric substrates

shown in Figure 18. The target dielectric is 200-nm  $\text{Si}_3\text{N}_4$ , deposited via low pressure chemical vapor deposition, on doped Si. We transferred the HOPG pillars by applying a large compression force  $>50$  N by sandwiching the HOPG pillars with  $\text{Si}_3\text{N}_4$  using a precision flattened vice. 30 V forward bias was applied to the HOPG, creating a 0.75 MPa electrostatic pressure force on 200 nm  $\text{Si}_3\text{N}_4$ , thus overcoming the 0.4 MPa needed for exfoliation from HOPG [22].

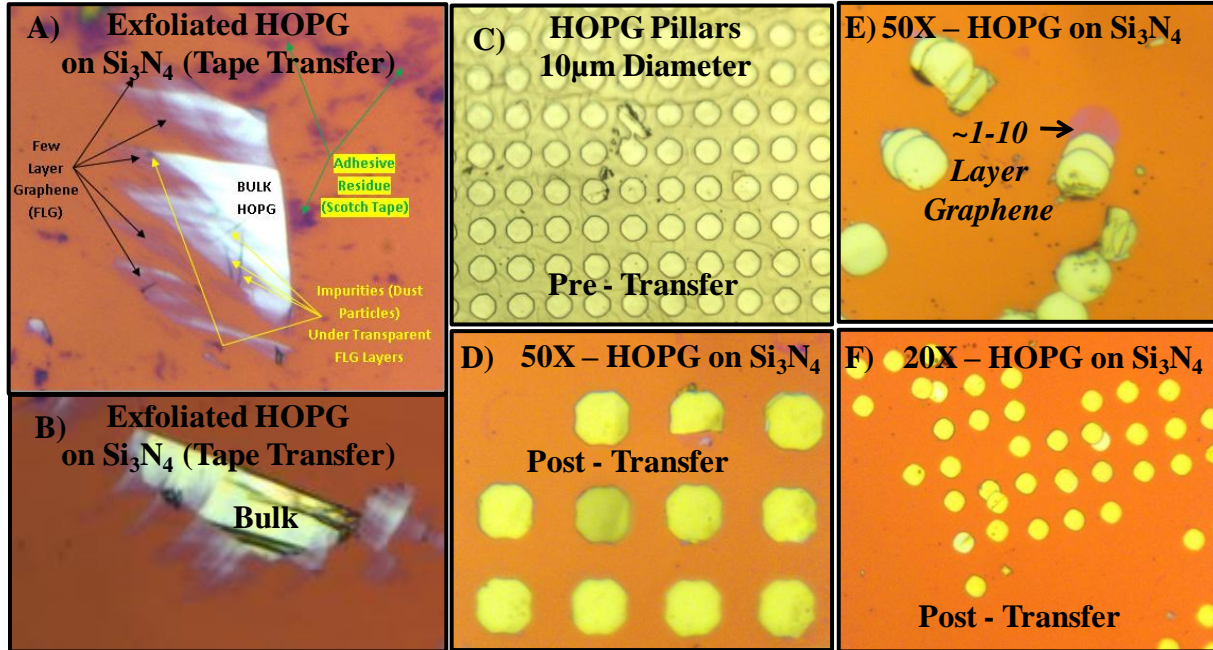


**Figure 18.** Various aspects of graphene transfer are outlined via optical microscopy; A) and B) are thin and bulk exfoliated graphite from HOPG bulk transferred to  $\text{Si}_3\text{N}_4$ , C) shows 10 $\mu\text{m}$  HOPG pillars, and D), E), F) are patterned HOPG pillars transferred to  $\text{Si}_3\text{N}_4$  substrate.

$\text{Si}_3\text{N}_4$  was chosen as the choice target substrate since this dielectric material can sustain high voltages before tunneling and can maintain strength under high pressures as compared with other substrates. Reliability test of current-voltage characterization for 200 nm of  $\text{Si}_3\text{N}_4$  was carried out until a tunneling regime of Poole-Frenkle emission [35,36] was clearly seen when compared with theoretical calculations shown in Figure 19A). The equation for this plot is labeled by Habermehl et al. in Ref [35]. Next, the electrostatic pressure force vs. voltage was plotted for  $\text{Si}_3\text{N}_4$  in Figure 19B) showing that a 0.4 MPa electrostatic pressure great enough to exfoliate HOPG can be accomplish at  $>22$ V. This plot shows that HOPG can be exfoliated between 22 V-80 V without venturing into the Poole-Frenkle emission tunneling arena that traps carrier charges. The electrostatic pressure calculation consists of  $P = \epsilon_0 \epsilon_r V^2 / 2d^2$ , where  $\epsilon_0$  is dielectric permittivity of free space  $8.85 \times 10^{-12}$  F/m,  $\epsilon_r$  is dielectric constant 7.5 for  $\text{Si}_3\text{N}_4$ ,  $d$  is thickness 200nm, and  $P$  is pressure in N/m.

Once fully characterized, the experimental apparatus was designed and built. Initially, we experienced problems with little to no exfoliation force. To seek out this problem we utilized a capacitance measurement technique to gauge how much of the HOPG was in contact with the  $\text{Si}_3\text{N}_4$  (contact area). This measurement revealed that the contact area between the two surfaces was much less than expected (a smaller capacitance). The solution to our problem was to use a

precision flat vice to clamp these plates together in excess of  $>100\text{N/m}$ . We were then able to achieve the correct capacitance within 5% and results of Figure 18 were then achieved in an ambient environment. Our results conclude that our apparatus relatively matches the electrostatic transfer quality of other setups found in literature and is ready to explore new research possibilities. We have yet to control the environmental conditions; therefore improvement to achieve high quality transfer is well in within the scope of this work.

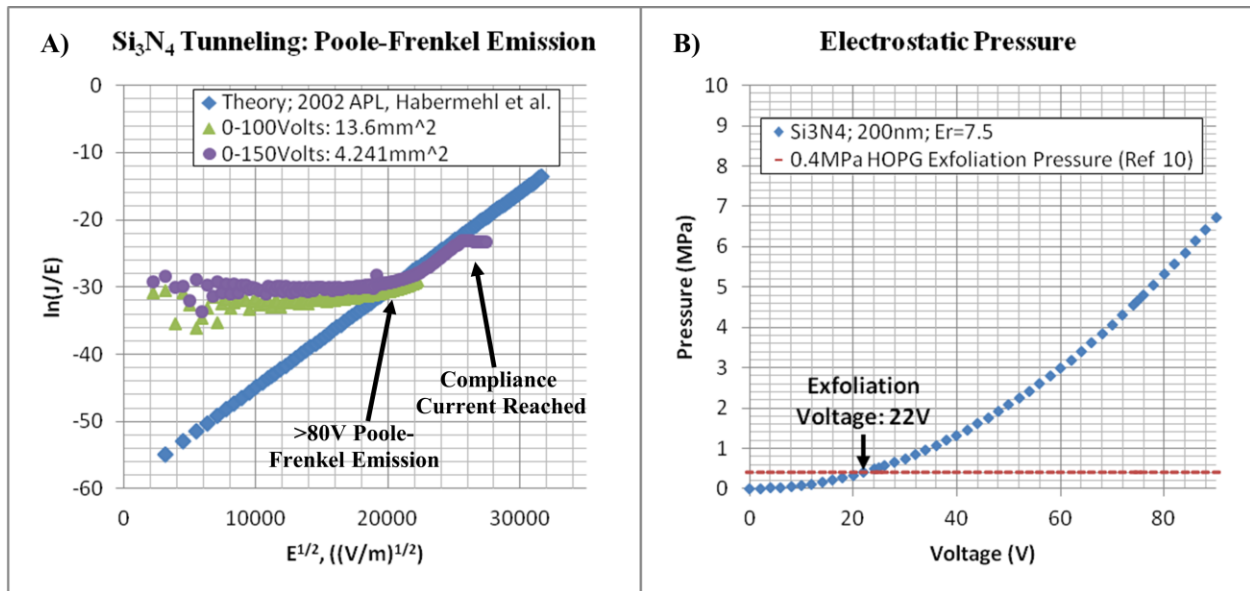


**Figure 19.** Reliability of 200 nm  $\text{Si}_3\text{N}_4$  as an electrostatic target substrate was carried out in A) where little carrier emission is seen up to 80 V and in B) 22 V was calculated to be the minimum voltage needed to achieve the 0.4 MPa HOPG exfoliation pressure.

## **5. FABRICATION OF GRAPHENE HALL BARS AND FIELD EFFECT TRANSISTORS**

To characterize the electronic properties of graphene synthesized by the thermal decomposition of SiC, several test structures were developed during this project. Graphene Hall bar structures were realized to measure graphene mobility and sheet resistance. Graphene FETs (GFETs) were fabricated to determine the location of the Dirac point and to demonstrate gate control of current conduction. The following sections describe the fabrication and characterization of these simple graphene devices.

### **5.1 Graphene Hall bar (GHB) fabrication**

The devices start with a SiC sample that is 5 mm x 12 mm square with varying thicknesses of graphene along the surface of the substrate. AZ5214 Photo Resist (PR) is used throughout this process to define the lithographic regions. The first lithography step defines the Hall bars using the PR. The sample is then etched using a SF<sub>6</sub>/O<sub>2</sub> in a Reactive Ion Etching (RIE) system in order to remove material 50-100 nm deep into the SiC substrate. With this process, graphene is left only within the bar regions of the sample. The PR is then removed using a 40 psi Acetone spray due to hardening of the PR during the etch process. One more step of lithography is then used to define the Ti/Au electrodes that are deposited using E-beam metal evaporation at a thickness of 3200 Å. PR from this step is then removed by soaking in acetone for lift off of the unwanted metal. Top down and cross sectional views are shown in Figure 20.

### **5.2 Graphene field effect transistor (GFET) fabrication**

Manufacturing of the GFET devices parallels the same process as described previously for the graphene Hall bar fabrication, and continues with additional steps. For example, after deposition of the source and drain electrodes, 500 nm of silicon oxide is deposited conformally using Physical Vapor Deposition (PVD) along the entire surface of the sample. A lithography step then defines the gate regions, and metal (Ti 200 Å/Au 3000Å) is evaporated followed by soaking in acetone to remove excess metal. To make sure that the oxide on the contact pads is removed, one last lithography step is used to define regions on the pads, and the oxide is etched on the contact pads only. Top down and cross sectional views are shown in Figure 21.

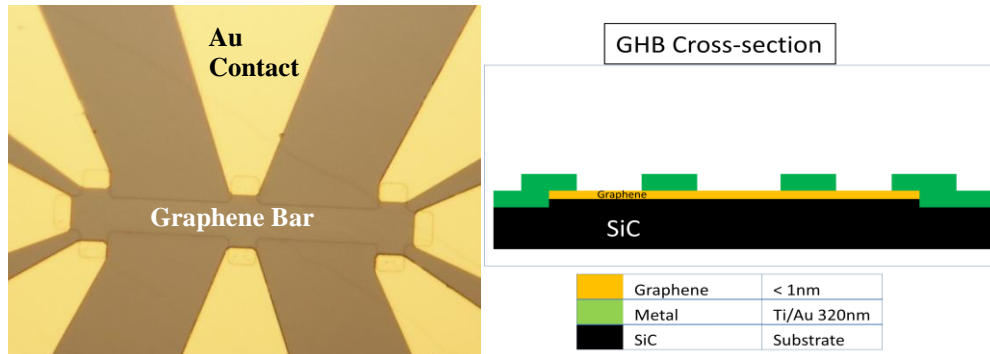


**Figure 20.** Optical top down image of graphene Hall bar and cross sectional side view.

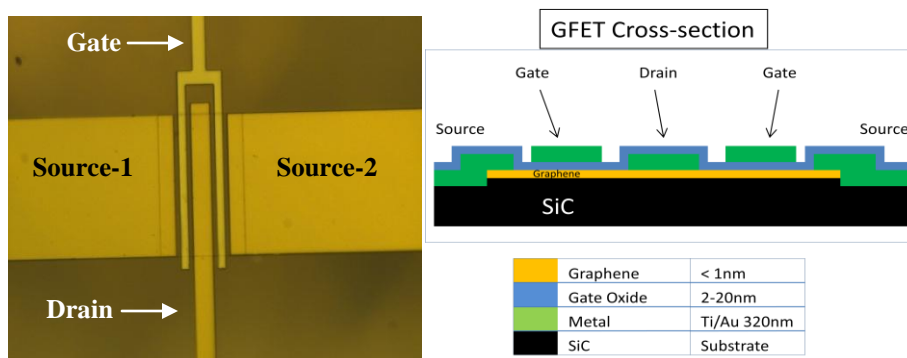


**Figure 21.** Optical top down image of GFET and cross sectional side view.

### 5.3 Characterization of Hall bars and GFETs

GFET and Hall bar structures were developed to characterize the electronic properties of graphene films grown by the thermal decomposition method discussed in section 2.1. A detailed discussion of graphene Hall bar characterization can be found in section 6.1. The remainder of this section will discuss characterization of GFETs fabricated from graphene grown on the silicon face of semi-insulating SiC.

GFETs are characterized electronically using two methods: 1) drain current ( $I_d$ ) is measured as a function of source-drain voltage ( $V_{ds}$ ) for different gate voltages ( $V_g$ ), 2)  $I_d$  is measured as a function of  $V_g$  at a constant  $V_{ds}$ . All electronic measurements were made at room temperature using an Agilent 4155B semiconductor parametric analyzer that has four independently controlled source measurement units (SMUs).

Figure 22 shows typical  $I_d(V_{ds})$  curves for different gate voltages. These data clearly show that the current in the graphene channel is modulated by the gate voltage. At higher  $V_g$  levels the  $I_d$  appears to saturate. Current modulation in the graphene is due to an increase or decrease in carrier density caused by the applied transverse electric field from the gate electrode [37]. A mechanism for the inflections present in  $I_d(V_{ds})$  data at lower  $V_g$  levels is explained in Ref. [37]. This inflection indicates the formation of an ambipolar channel, where carrier type changes somewhere along the graphene channel that is located under the gate electrode.

Figure 23 shows a typical  $I_d(V_g)$  plot for a GFET device. The location of the Dirac point can be clearly seen in the current minimum (typically close to -1V). The typical on/off ratio for our devices is approximately 2.

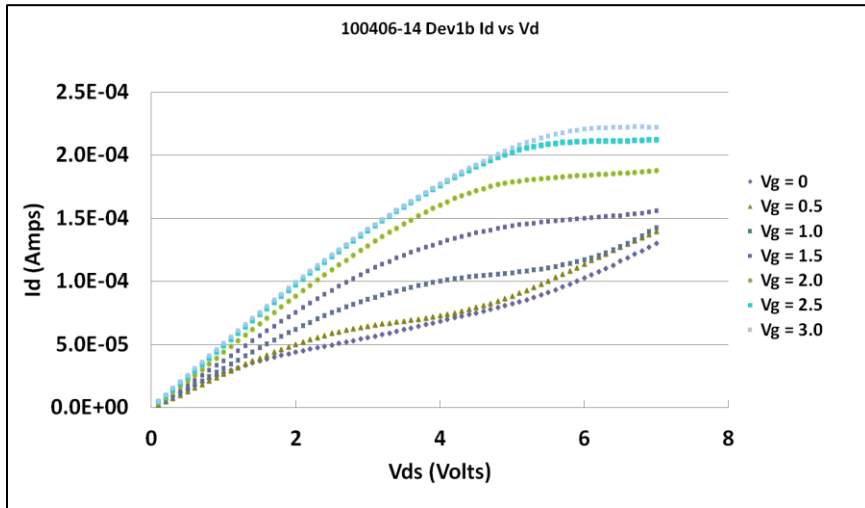


Figure 22. Typical  $I_d(V_{ds})$  curves for several  $V_g$  levels.

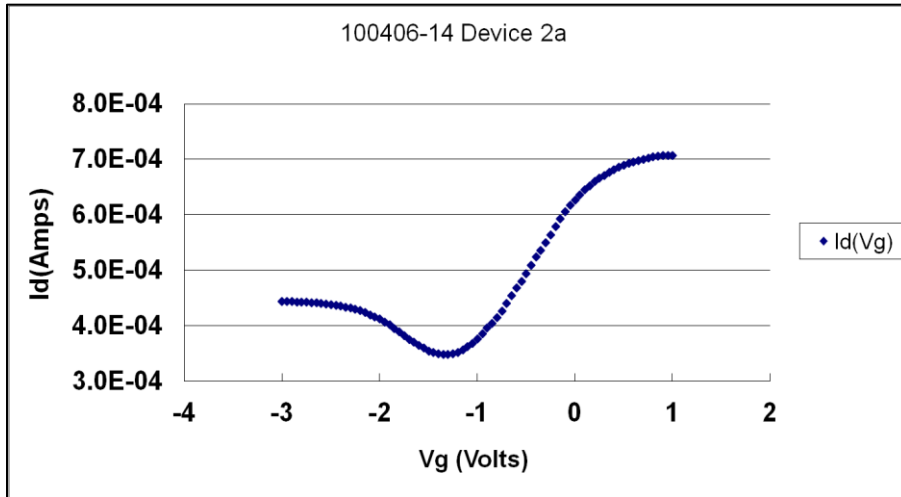


Figure 23.  $I_d(V_g)$  curve for a typical GFET.



## 6. LOW TEMPERATURE MAGNETO TRANSPORT

The unique electronic properties of graphene and its promising potential as a next generation electronic device material have stimulated the development of synthesis routes for improved film quality [1,38] and the research of its electron physics. In this session, we will present two main results: 1) Observation of the integer quantum Hall effect in high quality, uniform wafer-scale epitaxial graphene films; 2) Electron-electron interaction in high quality epitaxial graphene.

### 6.1 Observation of the integer quantum Hall effect in high quality, uniform wafer-scale epitaxial graphene films

Growth of high quality graphene films on SiC is regarded as one of the more viable pathways toward wafer-size graphene-based electronics, as graphene films form readily on SiC surfaces by vacuum sublimation of silicon (Si) at elevated temperature leaving behind a graphene film (a process termed “graphitization”) [39,40].

However, the quality of graphene films produced by this method is poor when compared to exfoliated samples and it is difficult to grow high quality, uniform wafer-size graphene layers. Furthermore, transport measurements reveal the quality of the two-dimensional electron gas (2DEG) is also poor, especially for films grown on the Si-face, and there has been no report of the integer quantum Hall effect (IQHE) [41]. Recently, a new approach that involves heating SiC in argon at atmospheric pressure has led to significant improvement in the domain size and electronic properties [3, 42] compared to vacuum graphitization [43]. In the past several months, several groups [44-47] were able to achieve high quality 2DEG in epitaxial graphene films and reported the observation of integer quantum Hall states.

In this section, we report low temperature magneto-transport and four-probe measurements of graphene films grown on the Si face of SiC produced via Ar-assisted graphitization. We have achieved a low temperature carrier mobility  $\sim 14,000 \text{ cm}^2/\text{Vs}$  at the electron density of  $6.1 \times 10^{11} \text{ cm}^{-2}$  in an as-grown film, which is comparable to that reported in exfoliated graphene on a substrate (non-suspended). Integer quantum Hall effect states at the Landau level fillings  $\nu=2,6,10$  were observed in a Hall bar device made of these epitaxial graphene films. Furthermore, four-probe measurements on a specimen grown under similar conditions show relatively uniform sheet resistance ( $\sim 1600 \text{ }\Omega/\text{square}$ ) across the whole wafer ( $12 \times 6 \text{ mm}^2$ ). These transport results combined with our microscopy characterization [48] reveal that atomic substrate steps and minor multilayer graphene domains minimally influence the mobility [47].

The graphene films are produced using a method similar to that reported in Refs. [3,42]. The samples studied here are grown on n-type 6H-SiC(0001) (Si-face,  $\sim 0.1 \text{ }\Omega\text{-cm}$ , Cree, Inc.). Prior to graphene growth, the surface was hydrogen etched (45%  $\text{H}_2$  – argon (Ar) mixture) at 1500-1600 °C to remove polishing damage and to produce extended wide atomic terraces of SiC. Graphene was grown in a high temperature furnace operated at atmospheric pressure. The sample temperature was raised to 1200°C in a 10%  $\text{H}_2$  – Ar mixture, then to 1500-1700 °C in an Ar atmosphere. To identify the thickness of the graphene layer, we have used the energy dependence of the specular electron reflection (LEEM-IV) of each domain [43,49]. In the specimen we observed the IQHE states, it was identified that 90% of the area is covered with

single layer graphene, and the rest with multilayer. In addition to LEEM, we have used AFM to determine the surface topography.

Conventional photolithographic techniques were used to fabricate the Hall bar structures.  $\text{SF}_6$  gas was used in a reactive ion etch chamber to both etch the graphene and up to 50 nm deep into the SiC substrate [50]. Ti/Au was then deposited to form metal contacts. Figure 24 shows a microscopic image of a typical Hall bar device. The inset shows 12 Hall bar structures of various sizes.

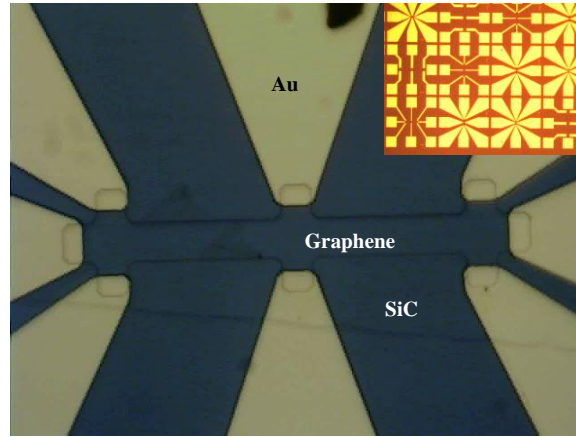


**Figure 24.** Microscopic image of a Hall bar device. Inset shows various devices of different sizes.

The low temperature magneto-transport measurements were carried out on three similarly sized devices ( $50 \times 6.25 \mu\text{m}^2$ ) in a pumped  $^3\text{He}$  system. In Figure 25, we show the longitudinal magneto-resistivity ( $\rho_{xx}$ ) and transverse Hall resistivity ( $\rho_{xy}$ ) measured at 4K in a typical device, after three thermal cycles between room temperature and 4K. Around  $B = 0$ , a weak-localization (WL) peak was observed. The formula developed in Ref. [51] was used to fit this WL peak and it yields a phase coherence length of  $\sim 0.7 \mu\text{m}$ . At higher magnetic field, pronounced Shubnikov de Haas (SdH) oscillations are clearly seen in  $\rho_{xx}$ . We assign each minimum (marked by the up-triangles in Figure 25(a)) an integer number ( $N$ ) and plot the conventional Landau fan diagram, i.e.,  $N$  versus  $1/B$ , in Figure 25(b). All the data points fall onto a straight line and the intercept at  $1/B = 0$  is  $1/2$ . The value of this intercept is the same as what was reported in Ref. [52,53] in exfoliated graphene and was taken as evidence of a single layer sample.

At even higher magnetic field,  $B > 8\text{T}$ ,  $\rho_{xx}$  becomes vanishingly small. In  $\rho_{xy}$ , a fully developed plateau with a quantized value of  $0.5 \times h/e^2$  is seen, demonstrating the formation of the  $\nu=2$  IQHE state. Hall plateaus are also seen around  $B \sim 4.5\text{T}$  ( $\rho_{xy} \sim 1/6 \times h/e^2$ ) and  $\sim 3\text{T}$  ( $\rho_{xy} \sim 1/10 \times h/e^2$ ), indicating the formation of the IQHE states at  $\nu=6$  and  $10$ , respectively. This unique sequence of IQHE states at  $\nu=2, 6, 10$  is a distinguishing signature of Dirac electrons in single layer graphene [17,18]. Examining Figure 25(a) more carefully, we note that the center of the Hall plateaus at  $\nu=6$  and  $10$  does not coincide with the  $R_{xx}$  minimum positions of the same filling factor. This kind of transport feature was also observed in the past in the 2DEG in GaAs/AlGaAs heterostructures [54] and believed to be due to an asymmetric density of state caused by charged impurities in the 2D channel, which are known to also exist in our graphene film.

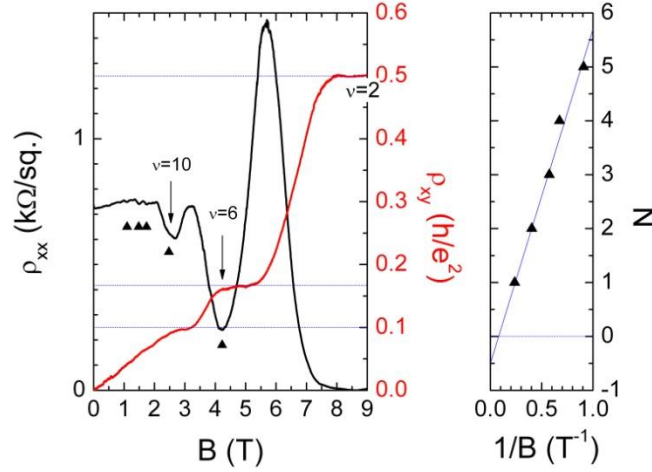


**Figure 25.** (a):  $\rho_{xx}$  and  $\rho_{xy}$  measured in a typical graphene Hall bar device. The sample temperature is 4 K. (b): Landau fan diagram for Shubnikov-de Haas oscillations.

Using the  $B$  value of the  $\rho_{xx}$  minimum of the  $\nu=6$  IQHE state, the 2DEG density is calculated to be  $n = 6.1 \times 10^{11} \text{ cm}^{-2}$ . This agrees well with that ( $\sim 6.0 \times 10^{11} \text{ cm}^{-2}$ ) obtained from the slope of the Hall resistance around  $B = 0$ . The as-grown electron density in this device is relatively low, almost a factor of two smaller compared to recent reports [44]. The resistivity at  $B = 0$  is  $\rho \sim 720 \text{ } \Omega/\text{square}$ . The electron mobility, determined by  $\mu=1/(ne\rho)$ , is  $\mu \sim 14,000 \text{ cm}^2/\text{Vs}$ . This value is consistent with that obtained from  $\mu B_0 \sim 1$ , where  $B_0 \sim 0.85 \text{ T}$  is the magnetic field at the onset of SdH oscillations, indicating that the dominant carrier scattering mechanism in this device is of short-range scattering. The high carrier mobility probably is due to the improvements of the Ar-assisted method used in our growth caused by a changed buffer layer surface morphology and, consequently, high quality, large-size monolayer graphene [4]. On the other hand, it can also be a density effect. Indeed, it has been shown in Ref. [46] that the carrier mobility can be increased to  $29,000 \text{ cm}^2/\text{Vs}$  at  $n = 5.4 \times 10^{10} \text{ cm}^{-2}$  from the as-grown values of  $\sim 2,300 \text{ cm}^2/\text{Vs}$  and  $n = 8.9 \times 10^{12} \text{ cm}^{-2}$ . In this regard, however, we notice that in Ref. [47] smaller mobilities, between  $4000$  and  $7500 \text{ cm}^2/\text{Vs}$ , were reported at similar electron densities in as-grown graphene films. Finally, our temperature dependent study of the zero magnetic field resistivity shows a weak temperature dependence below  $\sim 10 \text{ K}$ .

Magneto-transport measurements were also carried out on two other Hall bar devices of the same size on the same substrate. In both devices, the quantum Hall plateau was observed at  $\nu=2$  and  $6$ . Their 2DEG densities (mobilities) are  $\sim 4 \times 10^{11} \text{ cm}^{-2}$  ( $\sim 11,000 \text{ cm}^2/\text{Vs}$ ) and  $\sim 5 \times 10^{11} \text{ cm}^{-2}$  ( $\sim 10,000 \text{ cm}^2/\text{Vs}$ ), respectively. The density and mobility in these three different areas are similar, suggesting that a uniform whole-wafer epitaxial single graphene film has been achieved.

To further corroborate this claim, we have measured 12 Hall bar devices on a second sample that were fabricated on a graphene sample prepared under the same growth conditions as the first sample above. The sizes of the Hall bars are  $400 \times 50 \text{ } \mu\text{m}^2$ ,  $200 \times 25 \text{ } \mu\text{m}^2$ ,  $100 \times 12.5 \text{ } \mu\text{m}^2$  and  $50 \times 6.25 \text{ } \mu\text{m}^2$ . All the measurements were carried out at zero magnetic field in a Lakeshore Cryogenic probe station with the sample in vacuum. The sheet resistance ( $R_s$ ) was measured using a standard four probe configuration at  $\sim 4.2 \text{ K}$ . Typical source current sweeps ranged from

+100  $\mu\text{A}$  to -100  $\mu\text{A}$ . In this current range, a linear I-V was observed.  $R_s$  was then determined from a linear fit applied to the I-V data.

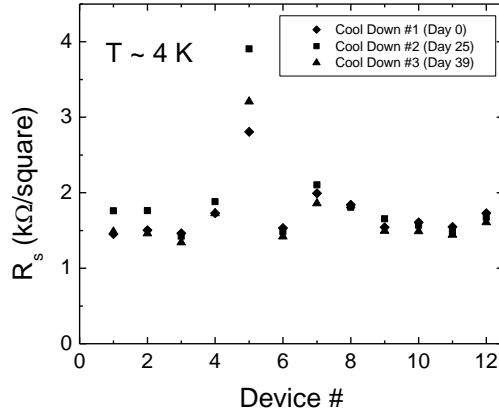


**Figure 26.**  $R_s$  measured for multiple devices over three cool-down cycles.

Figure 26 shows  $R_s$  for multiple devices over three different cool-down cycles. All devices, except for device # 5, showed a consistent  $R_s$  ( $\sim 1600 \Omega/\text{square}$ ) during each cool-down/measurement cycle. Using this value and assuming a 2DEG density of  $6 \times 10^{11} \text{ cm}^{-2}$ , we obtain an average mobility of  $\sim 6,500 \text{ cm}^2/\text{Vs}$  for this sample. This value is consistent with those obtained by other groups [44,45,47], and roughly a factor of two smaller than that in our first sample. Figure 4 shows the average  $R_s$  measure over several different days. The data in Figure 26 and Figure 27 clearly show no spatial dependence for  $R_s$ , as well as stability over time. The average  $R_s$  for all devices (excluding device #5) measured on different days are listed in the table inserted in Figure 27.

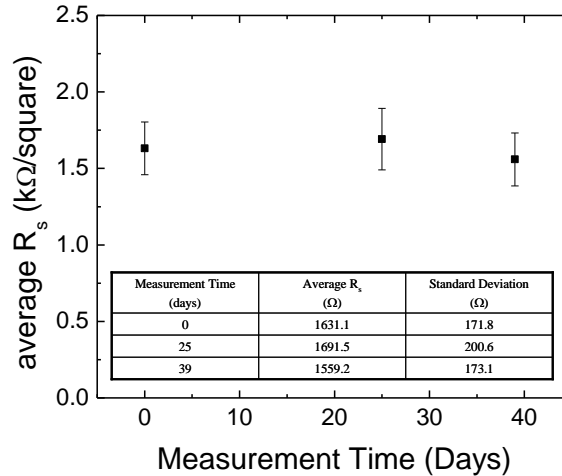


**Figure 27.** Average  $R_s$  data for eleven devices (excluding device #5) measured in multiple days.

In summary, the unique sequence of the integer quantum Hall effect states at  $\nu=2,6,10$  was observed in a high quality epitaxial graphene Hall bar device with an electron density  $6.1 \times 10^{11}$

$\text{cm}^{-2}$  and mobility  $\mu \sim 14,000 \text{ cm}^2/\text{Vs}$ . Our four-probe measurements at  $B = 0$  further suggest that the epitaxially grown graphene film is uniform across the whole wafer ( $12 \times 6 \text{ mm}^2$ ).

## 6.2 Electron-electron interaction in high quality epitaxial graphene

The ground state of a two-dimensional electron system (2DES) at  $T = 0$  is a subject of intense research for many years. In particular, electron transport properties in the presence of electron-electron (e-e) interactions remain as the center of current research [55]. With the arrival of graphene [1,38,56-58], new ground states induced by the combination of e-e interactions and massless Dirac fermions have been proposed [59]. Indeed, the 2DES in graphene may represent a novel two-dimensional (2D) Fermi liquid with unusual e-e interaction physics. Recent observations of the fractional quantum Hall effect at Landau level filling  $\nu = 1/3$  [60-62], many-body originated  $\nu = \pm 1$  states [63], and the e-e interaction-induced shift in the cyclotron resonance measurements [64] demonstrate that a yet rich, e-e interaction induced many-body physics still waits to be discovered in graphene at *high* magnetic ( $B$ ) fields.

In comparison, much less experimental work has been conducted to examine e-e interactions at *zero* and *low* magnetic fields, in particular, in epitaxial graphene films. In contrast, in an ordinary 2DES, extensive studies have been carried out in this region and it has been clearly established that e-e interactions play a non-trivial role in carrier conductivity in the so-called diffusive regime (or  $k_F l \gg 1$ , where  $k_F$  is the Fermi vector and  $l$  electron mean free path) [65], where Coulomb interaction is known to be enhanced between diffusively moving electrons. In this regard, it is important to experimentally study whether and how e-e interactions affect the graphene conductivity in the same regime [66-72].

In this session, we show that in epitaxially grown graphene, through a systematic study of weak-localization phenomenon at zero and low  $B$  fields, e-e interactions probably do impact the carrier conductivity in the diffusive regime and contribute a logarithmic temperature ( $T$ ) dependence term to the zero  $B$  field conductivity. Furthermore, our results indicate that the e-e interaction correction term developed for the ordinary 2DES needs to be modified for the 2DES in graphene.

Our measurements are carried out in two high quality epitaxial graphene films grown on the silicon-faced 6H-SiC substrates, using a method similar to that reported in Refs. [3,42]. Conventional photolithographic techniques were used to fabricate the Hall bar structures of size  $50 \times 6.25 \mu\text{m}^2$ . The conventional low-frequency phase lock-in technique was used for low temperature magneto-transport measurements. For sample A, the single layer graphene film is grown on an electron-type doped 6H-SiC (0001) and it has a low temperature density  $n \sim 6 \times 10^{11} \text{ cm}^{-2}$  and mobility  $\mu \sim 10,000 \text{ cm}^2/\text{Vs}$ . For sample B, the 6H-SiC(0001) substrate is counter-doped and insulating at room temperature. The low temperature density and mobility are  $n \sim 2.4 \times 10^{12} \text{ cm}^{-2}$  and  $\mu \sim 3700 \text{ cm}^2/\text{Vs}$ , respectively. At high magnetic fields, the integer quantum Hall states at Landau level fillings  $\nu = 2, 6, 10$  were observed in sample A. In sample B, Shubnikov-de Haas oscillation minima were observed at  $\nu = 10, 14, 18$ , and up to  $\nu = 34$ .

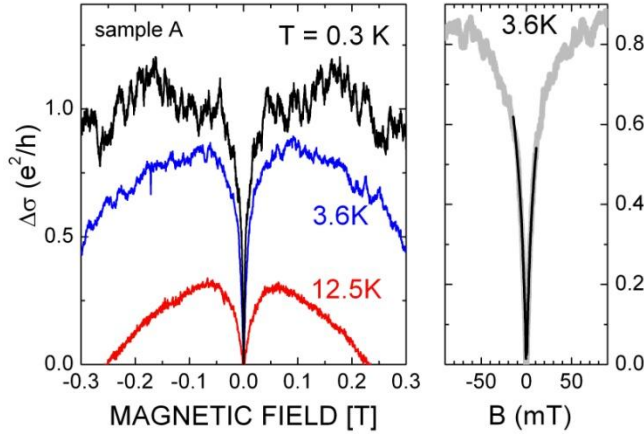


**Figure 28.** (a) magneto-conductive,  $\Delta\sigma(B) = \sigma_{xx}(B) - \sigma_{xx}(0)$  at three temperatures for sample A. (b) weak-localization fitting to the  $T = 3.6\text{K}$  data. The gray line is the experimental data. The black line is the fitting.

Figure 28(a) shows  $\Delta\sigma(B) = \sigma_{xx}(B) - \sigma_{xx}(0)$  for sample A at three selected temperatures.  $\sigma_{xx}(B)$  is the magneto-conductivity, deduced according to the formula  $\sigma_{xx}(B) = \rho_{xx}(B)/(\rho_{xx}(B)^2 + \rho_{xy}(B)^2)$ , where  $\rho_{xx}(B)$  is the diagonal magneto-resistivity and  $\rho_{xy}(B)$  is the Hall resistivity.  $\sigma_{xx}(0) = 1/\rho_{xx}(0)$  is the conductivity at  $B = 0$ . The weak-localization (WL) phenomenon is observed at all three temperatures and  $\Delta\sigma(B)$  decreases as  $B$  approaches zero from both directions. We point out here that to fully reveal this weak-localization phenomenon a very slow rate, 1 Tesla per 100 minutes, was used for magnetic field sweep. A faster sweep rate would reduce the amplitude of WL peaks. At the lowest temperature ( $T$ ) of  $T = 0.3\text{K}$ , strong universal conductance fluctuations (UCF) are also seen and their amplitude decreases with increasing temperature [4]. By  $T = 12.5\text{K}$ , UCF almost disappears in this sample.

WL in graphene has been reported in previous studies [44,47,73-80] and is shown to be due to the quantum interference effect of impurity scattering [51]. Figure 28(b), we show a WL fitting to the trace at  $T = 3.6\text{K}$  according to the formula developed by McCann et al. [51],  $\Delta\sigma(B) = \alpha \times e^2/\pi h \times [F(B/B_\phi) - F(B/(B_\phi + 2B_i)) - 2F(B/(B_\phi + B_i + B_*))]$ , where  $F(z) = \ln z + \Psi(1/2 + 1/z)$ ,  $\Psi$  is the digamma function, and  $B_{\phi,i,*} = \hbar/4De\tau_{\phi,i,*}$ .  $D$  is the diffusion constant. This fitting allows us to deduce the following parameters relevant to electron transport in graphene, the phase-decoherence time (length)  $\tau_\phi$  ( $l_\phi$ ), inter-valley scattering time (length)  $\tau_i$  ( $l_i$ ) and intra-valley scattering time  $\tau_*$  ( $l_*$ ). We also include in our data fitting a coefficient  $\alpha$ ;  $\alpha$  equals to 1 in graphene.

We shall note here that the WL fitting in our samples was carried out within the so-called transport B field ( $B_{tr} = \hbar/4De\tau \sim 20\text{mT}$  in sample A,  $\tau$  the transport time) where the weak-localization effect is the strongest. Moreover, we have observed that  $\alpha$  and  $B_\phi$  in our fitting are nearly independent of the values of  $B_i$  and  $B_*$ , which can be varied over a very large range, as long as  $B_{i,*} \gg B_\phi$  (or  $\tau_{i,*} \ll \tau_\phi$ ). Our final WL fitting results were obtained with two more constrains: 1)  $\tau_\phi^{-1} + \tau_i^{-1} + \tau_*^{-1} \sim \tau^{-1}$  and 2)  $\alpha$  equals to 1 within  $\pm 5\%$ .

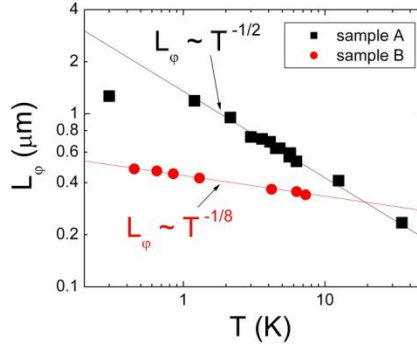


**Figure 29.**  $l_\phi$  versus  $T$  for sample A (squares) and samples B (dots).

In Figure 29, the temperature dependence of phase coherent length ( $l_\phi$ ) for sample A (squares), determined by  $l_\phi = (D\tau_\phi)^{1/2}$ , is plotted. Between 1 and  $\sim 30$  K,  $l_\phi$  displays a power law dependence on temperature and  $l_\phi \sim T^{-1/2}$ , consistent with some previous studies [74,75]. Below 1 K,  $l_\phi$  saturates to a value of  $\sim 1 \mu\text{m}$ . This saturation is unlikely due to electron heating. A very small excitation current, 1 nA, corresponding to an input power of  $10^{-15}$  W, was used for the conductivity measurements. Rather, we believe that it is due to a finite domain size of graphene terraces resulting from the graphitization process. Our low energy electron diffraction microscopy measurements on a graphene sample grown under similar conditions seem to support this proposal. From the temperature dependence of  $l_\phi \propto T^{-1/2}$ ,  $\tau_\phi = l_\phi^2/D \propto T^{-1}$  is then deduced. This  $T^{-1}$  dependence indicates that the electron-electron scattering process is the dominant dephasing mechanism in sample A [74]. The intervalley scattering length ( $l_i = (D\tau_i)^{1/2}$ ) and intravalley scattering length ( $l_* = (D\tau_*)^{1/2}$ ) are  $\sim 100$  nm and they are temperature independent, consistent with previous work [44,47,73-80].

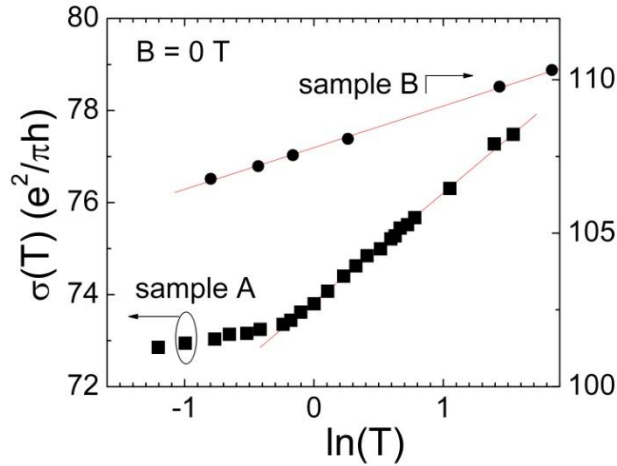


**Figure 30.** Zero B field conductivity versus  $\ln(T)$  for sample A (squares) and sample B (dots).

Having studied the weak-localization phenomenon at low B fields, we now concentrate on the zero B field conductivity data. Its temperature dependence is shown in Figure 30. There, the conductivity (solid squares, in units of  $e^2/\pi h$ ) is plotted as a function of  $\ln(T)$ . For  $T > 1$  K, a logarithmic temperature dependence of conductivity is clearly observed. Below 1 K, the

temperature dependence becomes much weaker. We believe that this weak dependence at  $T < 1$  K is probably related to the saturation of  $l_\phi$  seen in Figure 29.

To fit this logarithmic T-dependent data, we again use the formula developed in Ref. [51] for non-interacting electrons in graphene. This formula can be simplified for our samples considering  $\tau_\phi \gg \tau \gg \tau_i \sim \tau^*$ . The final equation we use for fitting is given by  $\sigma(T) = p \times e^2/\pi h \times \ln(T) + \text{constant}$ , where  $p$  is the scaling parameter in  $\tau_\phi \propto T^{-p}$ . We shall note that the phonon contribution to the conductivity is not corrected in our fitting. This is justified since the phonon contribution is very small in the temperature range we carried out the measurements. The straight line in Figure 30 is a linear fit. From the slope of the line,  $p \approx 2.3$  is obtained.

$p \approx 2.3$  is much larger than the value of  $p = 1$  we obtained from the temperature dependence of  $l_\phi$ . This discrepancy strongly indicates the existence of another mechanism that can also produce a logarithmic temperature correction to the electron conductivity. In this regard, we note that it has long been known that in the ordinary 2DES e-e interactions contributes a logarithmic T dependent correction to the electron conductivity at zero B field [81], with an amplitude of the same order as that due to the quantum interference effect. It is possible that this interaction correction also plays a similar role in carrier conductivity in graphene. We therefore adopt the e-e interaction correction term  $\delta\sigma = [1 + 3(1 - \ln(1 + F_0^\sigma)/F_0^\sigma)] \times e^2/\pi h \times \ln(k_B T \tau/\hbar)$  [65,82], where  $F_0^\sigma$  is a measure of e-e interaction. With this new interaction correction term and using  $p=1$  obtained from the T-dependence of  $l_\phi$ ,  $F_0^\sigma \sim 0.23$  is deduced for sample A.

A smaller but again positive  $F_0^\sigma$  value is obtained in sample B with higher carrier density. Its low T magneto-resistivity  $\rho_{xx}$  trace taken at 4K is shown in Figure 31, and Shubnikov-de Haas (SdH) oscillations are seen up to Landau level filling  $\nu=34$ . From the positions of the SdH oscillation minima, an electron density,  $\sim 2.4 \times 10^{12} \text{ cm}^{-2}$ , is deduced. This value is consistent with that obtained from the low B field Hall resistance (not shown). The insert of Figure 31 shows the weak-localization phenomenon around  $B = 0$ , from which  $\tau_\phi$ ,  $\tau_i$ , and  $\tau^*$  (or  $l_\phi$ ,  $l_i$ , and  $l^*$ ) can be obtained. The temperature dependence of  $l_\phi$  for sample B (dots) is shown in Figure 29. Unlike in sample A,  $l_\phi$  in sample B shows a much weaker temperature dependence,  $l_\phi \propto T^{-1/8}$ .

Consequently, a weaker T dependence for  $\tau_\phi$ ,  $\tau_\phi \propto T^{-1/4}$  (or  $p = 1/4$ ), is obtained. This weak T dependence for  $\tau_\phi$  (or  $l_\phi$ ) has also been observed in graphene films with high 2DES density [44,76] and it suggests that de-coherence mechanisms other than e-e scattering may be important. The zero field temperature dependence for sample B (dots) is shown in Figure 30. Again, a logarithmic temperature dependence is observed for this sample. Similar to sample A, a larger  $p$  ( $p \sim 1.3 \gg 1/4$ ) would have been obtained from the linear fit if the electron-electron interaction term is not included in data fitting. With the interaction correction term, a value of  $F_0^\sigma \sim 0.08$  is deduced.

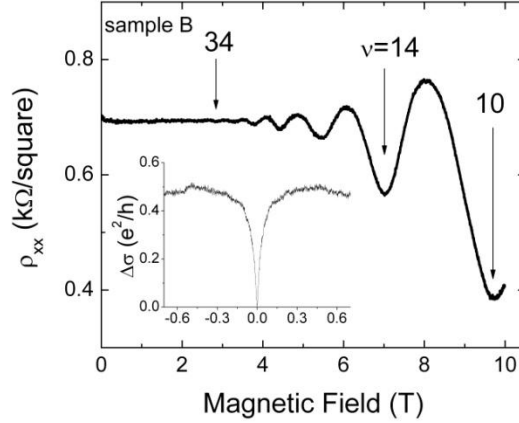


**Figure 31.**  $\rho_{xx}$  versus B for sample B. The insert shows  $\Delta\sigma(B)$  around  $B = 0$ .

We emphasize here that our data demonstrate that a new term with a logarithmic T dependence, probably due to electron-electron interaction, has to be included to the zero B field conductivity in order to resolve the discrepancy in the value of  $\nu$  obtained from the zero B measurements and low-field magneto-resistivity measurements. However, a positive value in  $F^{\sigma}_0$ , a measure of e-e interaction, is obtained if we use the formula derived for the ordinary 2DES. This unphysical value strongly suggests that the formula developed for the ordinary 2DES needs to be modified for 2DES in graphene. This is possible since a new type of Fermi liquid with novel electron physics has been suggested for electrons in graphene [71]. In general, the self-energy of a fermionic system consists two parts, the exchange contribution due to e-e interactions and a correlation contribution due to quantum fluctuations of the Fermi sea [83]. In graphene films, due to the chirality of Dirac fermions, it is highly likely that the e-e interaction correction term differs from the ordinary 2DES.

Finally, we note that in a recent study [84] the effect of electron-electron interaction was investigated in graphene films fabricated by mechanical exfoliation method. The authors showed that their results could be understood under the model developed for ordinary 2DES. It is not known to us what exactly is responsible for this discrepancy between the two experiments. On the other hand, different techniques, i.e., exfoliation versus epitaxial growth, were used in obtaining the graphene films in these two experiments. It is possible that the strength of e-e interaction is different in these different types of graphene films. Perhaps in our graphene devices, contributions from the  $2k_F$  scattering cannot be omitted in determining the electron screening [58], which, in turn, is responsible the observed discrepancy in the two kinds of samples.

To summarize, the weak localization phenomenon was studied in two high quality epitaxial graphene films grown on the silicon-faced 6H-SiC substrates at zero and low magnetic fields. Our results show that a new logarithmic temperature dependent term, probably due to electron-electron interactions, has to be taken into account. Furthermore, our results show that the interaction correction term developed for ordinary 2DES needs to be modified for the 2DES in graphene.



## 7. CONCLUSIONS

During this project, the Sandian graphene team has established leadership in graphene research community by addressing the key science issues impeding the synthesis of defect-free large area graphene films. Developing a fundamental understanding of synthesis will facilitate graphene's integration into advanced nanoscale devices and emerging nanoelectronic applications.

Several key accomplishments from this project are:

- Developed graphene synthesis on SiC using atmospheric Ar and high temperature
  - Achieved domain size of  $100 \mu\text{m}^2$
  - Observed record electron mobility ( $14000 \text{ cm}^2/\text{Vs}$ )
  - Achieved excellent electronic uniformity across sample
  - Developed understanding of mechanisms for graphene growth on SiC
  - Developed strategy for bilayer graphene wafer scale growth
- Developed graphene growth by depositing carbon on SiC
- Developed process to synthesize graphene on Cu foils
- Observed Integer Quantum Hall Effect in multiple devices
- Developed a scalable process to transfer graphene from SiC (000-1) to Pyrex
- Fabricated GFET devices with room temperature operation

We believe these results will enable: 1) advanced understanding of graphene synthesis on SiC and Cu foil, improving film quality and uniformity, 2) scientific understanding of how domain size/quality depends on growth parameters, 3) improved understanding of electron transport in graphene grown on SiC, 4) direct positioning and transferring of graphitic material on relevant substrates, 5) advanced fabrication of novel electronic devices that exploit quantum mechanical effects.



## 8. REFERENCES

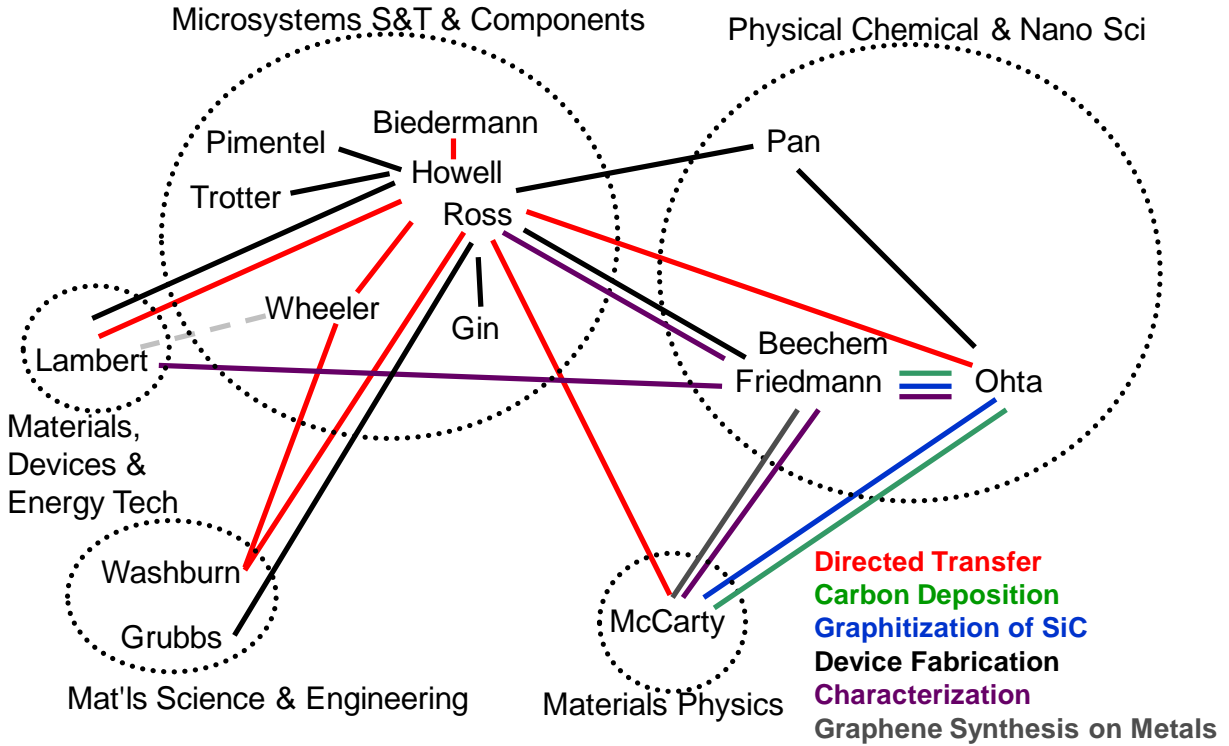
1. Geim, A. K. & Novoselvo, K. S., *Nature Mater.*, 2007, Vol. 6, p. 183\_191.
2. Berger, C. et al., *J. Phys. Chem. B*, 2004, Vol. 108, pp. 19912-19916.
3. Emtsev, et al., *Nature Materials*, 2009, Vol. 8, p. 203.
4. Ohta, et al. 2010, *Phys. Rev. B*, Vol. 81, p. 121411.
5. D. A. Schmidt, Taisuke Ohta, and T. E. Beechem, submitted.
6. Riedl et al., *Phys. Rev. Lett.* 103, 246804, 2009.
7. Lee et al., *Nano Letters*, published online, 2011.
8. S. Nie, A. L. Walter, N. C. Bartelt, E. Starodub, A. Bostwick, E. Rotenberg and K. F. McCarty, *ACS Nano* **5**, 2298-2306 (2011).
9. E. Starodub, A. Bostwick, L. Moreschini, S. Nie, F. El Gabaly, K. F. McCarty and E. Rotenberg, *Phys. Rev. B* **83** (2011).
10. Y. Murata, E. Starodub, B. B. Kappes, C. V. Ciobanu, N. C. Bartelt, K. F. McCarty and S. Kodambaka, *App. Phys. Lett.* **97** (2010).
11. J. M. Wofford, S. Nie, K. F. McCarty, N. C. Bartelt and O. D. Dubon, *Nano Lett.* **10**, 4890 (2010).
12. S. Nie, J. M. Wofford, N. C. Bartelt, O. D. Dubon and K. F. McCarty, *Phys. Rev. B*, *accepted* (2011).
13. J. M. Wofford, S. Nie, E. Starodub, A. L. Walter, A. Bostwick, K. Thurmer, N. C. Bartelt, E. Rotenberg, K. F. McCarty and O. D. Dubon, *Nano Lett.*, *submitted* (2011).
14. M. S. Fuhrer, C.N. Lau, and A.H. MacDonald, *MRS Bulletin*, 2010. 35(4): p. 289-295.
15. T. Palacios, A. Hsu, and H. Wang, *IEEE Communications Magazine*, 2010. 48(6): p. 122-128.
16. A. Reina, et al., *Nano Letters*, 2009. 9(1): p. 30-35.
17. D. S. Lee, et al., *Nano Letters*, 2008. 8(12): p. 4320-4325.
18. J. D. Caldwell, et al., *ACS Nano*, 2010. 4(2): p. 1108-1114.
19. S. Unarunotai, et al., *ACS Nano*, 2010. 4(10): p. 5591-5598.
20. A. Shukla, et al., 2009. 149(17-18): p. 718-721.
21. A. N. Sidorov, et al., *Nanotechnology*, 2007. 18(13): p. 135301.
22. X. Liang, et al., *Nano Letters*, 2009. 9(1): p. 467-472.
23. G. Wallis, and D. Pomerantz, *Journal of Applied Physics*, 1969. 40(10): p. 3946-9.
24. L. B. Biedermann, et al., *New Journal of Physics*, 2010. 12: p. 125016.
25. A. C. Ferrari, et al., 2006. 97(18): p. 187401.
26. L. M. Malard, et al., 2009. 473(5-6): p. 51-87.
27. D. Sun, et al., *Physical Review Letters*, 2010. 104(13): p.136802.
28. R. Yang, et al., *Journal of Applied Physics*, 2010. 107(3): p. 034305.
29. W. Pan, et al., *Applied Physics Letters*, 2010. 97: p. 2521
30. X. Li, W. Cai, J. An, S. Kim, J. Nah, D. Yang, R. Piner, A. Velamakanni, I. Jung, E. Tutuc, S. K. Banerjee, L. Colombo, and R. S. Ruoff, [Science](#) **324**, 1312-1314 (2009).
31. X. Li, Y. Zhu, W. Cai, M. Borysiak, B. Han, D. Chen, R. D. Piner, L. Colombo and R. S. Ruoff, [Nano Letters](#) **9** (12), 4359-4363 (2009).

32. A. Reina, H. Son, L. Jiao, B. Fan, M. S. Dresselhaus, Z. Liu, and J. Kong, [The Journal of Physical Chemistry C \*\*112\*\* \(46\), 17741-17744 \(2008\).](#)
33. W. Regan, N. Alem, B. Alemán, B. Geng, C. Girit, L. Maserati, F. Wang, M. Crommie, and A. Zettl, [Applied Physics Letters \*\*96\*\*, 113102 \(2010\).](#)
34. X. Liang, Z. Fu, and S. Y. Chou, [Nano Letters \*\*7\*\* \(12\), 3840-3844 \(2007\).](#)
35. S. Habermehl and C. Carmignani, [Applied Physics Letters \*\*80\*\*, 2, 14 \(2002\).](#)
36. S. Habermehl, R. T. Apodaca, and R. J. Kaplar, [Applied Physics Letters \*\*94\*\*, 012905 \(2009\).](#)
37. I. Meric, M. Han, A. Young, B. Ozyilmaz, P. Kim and K. Shepard, *Nature Nanotech.* **3**, 654 (2008).
38. W. A. de Heer, C. Berger, X. Wu, P.N. First, E.H. Conrad, X. Li, T. Li, M. Sprinkle, J. Hass, M.L. Sadowski, M.Potemski, G. Martinez, *Solid State Communications* **142**, 92 (2007).
39. I. Forbeaux, J. M. Themlin, and J. M. Debever, *Phys. Rev. B* **58**, 16396 (1998).
40. C Berger, Z. Song, X. Li, X. Wu, N. Brown, C. Naud, D. Mayou, T. Li, J. Hass, A. N. Marchenkov, E. H. Conrad, P. N. First, and W. A. de Heer, *Science* **312**, 1191 (2006).
41. P. Darancet, N. Wipf, C. Berger, W.A. de Heer, and D. Mayou, *Phys. Rev. Lett.* **101**, 116806 (2008).
42. C. Virojanadara, M. Syväjarvi, R. Yakimova, and L. I. Johansson, A. A. Zakharov, and T. Balasubramanian, *Phys. Rev. B* **78**, 245403 (2008).
43. T. Ohta, F. El Gabaly, A. Bostwick, J. L. McChesney, K. V. Emtsev, A. K. Schmid, T. Seyller, K. Horn, and E. Rotenberg, *New Journal of Physics* **10**, 023034 (2008).
44. T. Shen, J.J. Gu, M. Xu, Y.Q. Wu, M.L. Bolen, M.A. Capano, L.W. Engel, and P.D. Ye, *Appl. Phys. Lett.* **95**, 172105 (2009).
45. J. L. Tedesco, B. L. VanMil, R. L. Myers-Ward, J. M. McCrate, S. A. Kitt, P. M. Campbell, G. G. Jernigan, J. C. Culbertson, C. R. Eddy, Jr., and D. K. Gaskill, *Appl. Phys. Lett.* **95**, 122102 (2009).
46. J. Jobst, D. Waldmann, F. Speck, R. Hirner, D. K. Maude, T. Seyller, and H. B. Weber, *Phys. Rev. B* **81**, 195434 (2010).
47. A. Tzalenchuk, S. Lara-Avila, A. Kalaboukhov, S. Paolillo, M. Syväjärvi, R. Yakimova, O. Kazakova, T.J.B.M. Janssen, V. Fal'ko, and S. Kubatkin, *Nature Nanotechnology* **5**, 186 (2010).
48. unpublished.
49. H. Hibino, H. Kageshima, F. Maeda, M. Nagase, Y. Kobayashi, and H. Yamaguchi, *Phys. Rev. B* **77**, 075413 (2008)
50. M. Kothandaraman, D. Alok, and B.J. Baliga, *Journal of Electronic Materials* **25**, 875 (1996).
51. E. McCann, K. Kechedzhi, Vladimir I. Fal'ko, H. Suzuura, T. Ando, and B.L. Altshuler, *Phys. Rev. Lett.* **97**, 146805 (2006).
52. K. S. Novoselov, A. K. Geim, S. V. Morozov, D. Jiang, M. I. Katsnelson, I. V. Grigorieva, S. V. Dubonos, and A. A. Firsov, *Nature* **438**, 197 (2005).
53. Y. Zhang, Y.-W. Tan, H. L. Stormer, and P. Kim, *Nature* **438**, 201 (2005).
54. R.J. Haug, K.v. Klitzing, and K. Ploog, *Phys. Rev. B* **35**, 5933 (1987).

55. B. Spivak, S. V. Kravchenko, S. A. Kivelson, and X. P. A. Gao, *Rev. Mod. Phys.* **82**, 1743 (2010).
56. A.H. Castro Neto, F. Guinea, N.M.R. Peres, K.S. Novoselov, and A.K. Geim, *Rev. Mod. Phys.* **81**, 109 (2009).
57. N.M.R. Peres, *Rev. Mod. Phys.* **82**, 2673 (2010).
58. S. Das Sarma, S. Adam, E.H. Hwang, and E. Rossi, arXiv:1003.4731v2, unpublished.
59. For a recent review on electron-electron interactions in graphene, see, for example, V.N. Kotov, B. Uchoa, V. M. Pereira, A.H. Castro Neto, F. Guinea, arXiv:1012.3484, unpublished.
60. Xu Du, Ivan Skachko, Fabian Duerr, Adina Luican, and Eva Y. Andrei, *Nature* **462**, 192-195 (2009).
61. K.I. Bolotin, F. Ghahari, M.D. Shulman, H.L. Stormer, and P. Kim, *Nature* **462**, 196 (2009).
62. Wenzhong Bao, Zeng Zhao, Hang Zhang, Gang Liu, Philip Kratz, Lei Jing, Jairo Velasco, Jr., Dmitry Smirnov, and Chun Ning Lau, *Phys. Rev. Lett.* **105**, 246601 (2010)
63. Z. Jiang, Y. Zhang, H.L. Stormer, and P. Kim, *Phys. Rev. Lett.* **99**, 106802 (2007).
64. E. A. Henriksen, P. Cadden-Zimansky, Z. Jiang, Z. Q. Li, L.-C. Tung, M. E. Schwartz, M. Takita, Y.-J. Wang, P. Kim, H. L. Stormer, *Phys. Rev. Lett.* **104**, 067404 (2010).
65. G. Zala, B. N. Narozhny, and I. L. Aleiner, *Phys. Rev. B* **64**, 214204 (2001).
66. D.V. Khveshchenko, *Phys. Rev. Lett.* **97**, 036802 (2006).
67. A.F. Morpurgo, F. Guinea, *Phys. Rev. Lett.* **97**, 196804 (2006).
68. P.M. Ostrovsky, I.V. Gornyi, and A.D. Mirlin, *Phys. Rev. B* **74**, 235443 (2006).
69. C. Toke and J.K. Jain, *Phys. Rev. B* **76**, 081403 (2007).
70. K. Nomura and A.H. MacDonald, *Phys. Rev. Lett.* **98**, 076602 (2007).
71. M. Polini, R. Asgari, Y. Barlas, T. Pereg-Barnea, and A.H. MacDonald, *Solid State Commun.* **143**, 58 (2007).
72. J.H. Wang, H.A. Fertig, and G. Murthy, *Phys. Rev. Lett.* **104**, 186401 (2010).
73. S.V. Morozov, K.S. Novoselov, M.I. Katsnelson, F. Schedin, L.A. Ponomarenko, D. Jiang, and A.K. Geim, *Phys. Rev. Lett.* **97**, 016801 (2006).
74. X.S. Wu, X.B. Li, Z.M. Song, C. Berger, W.A. de Heer, *Phys. Rev. Lett.* **98**, 136801 (2007).
75. F.V. Tikhonenko, D.W. Horsell, R.V. Gorbachev, A.K. Savchenko, *Phys. Rev. Lett.* **100**, 056802 (2008).
76. D.K. Ki, D. Jeong, J.H. Choi, H.J. Lee, and K.S. Park, *Phys. Rev. B* **78**, 125409 (2008).
77. J. Moser, H. Tao, R. Roche, F. Alzina, C.M. Sotomayor Torres, and A. Bachtold, *Phys. Rev. B* **81**, 205445 (2010).
78. H.L. Cao, Q.K. Yu, L. A. Jauregui, J. Tian, W. Wu, Z. Liu, R. Jalilian, D. K. Benjamin, Z. Jiang, J. Bao, S. S. Pei, and Yong P. Chen, *Appl. Phys. Lett.* **96**, 122106 (2010).
79. M.B. Lundberg and J.A. Folk, *Phys. Rev. Lett.* **105**, 146804 (2010).
80. Y.M. Oh, J.H. Eom, H.C. Koo, and K.H. Han, *Solid State Communications* **150**, 1987 (2010).
81. B.L. Altshuler, A.G. Aronov, and P.A. Lee, *Phys. Rev. Lett.* **44**, 1288 (1980).

82. Due to a very fast inter-valley scattering rate, our graphene system can be viewed as an effective single-valley system.
83. M. Polini, R. Asgari, G. Borghi, Y. Barlas, T. Pereg-Barnea, and A.H. MacDonald, *Phys. Rev. B* **77**, 081411 (2008).
84. A. A. Kozikov, A. K. Savchenko, B. N. Narozhny, and A. V. Shytov, *Phys. Rev. B* **82**, 075424 (2010).

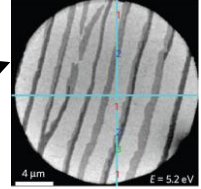
# APPENDIX A: SNL'S GRAPHENE TEAM NETWORK



## APPENDIX B: SUMMARY OF MAJOR ACCOMPLISHMENTS

- Sandia is established as a technical leader in the graphene community
  - Produced several high impact publications and presentations

- Achieved large area (~ 100  $\mu\text{m}^2$ ) synthesis on SiC through improved science-based understanding of growth mechanics



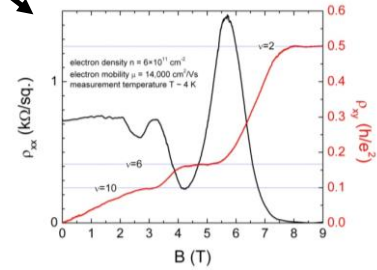
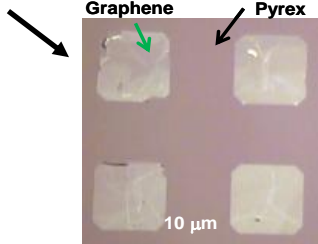
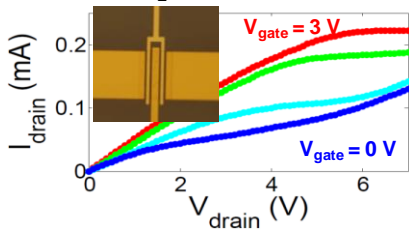
- Developed graphene synthesis using carbon deposition on SiC
- Demonstrated CVD graphene synthesis on Cu Foils
- Studied growth mechanisms for graphene synthesis on metals



- Developed wafer-scale bilayer synthesis approach
- Observed record mobility (14,000  $\text{cm}^2/\text{Vs}$ ) for epitaxial graphene
- Observed IQHE in several devices

- Demonstrated controlled transfer of graphitic material

- Fabricated 1<sup>st</sup> generation GFETS



## DISTRIBUTION

1	MS0868	Thomas Zipperian	Org. 2700
8	MS0892	Stephen Howell	Org. 1748
4	MS0892	Laura Biedermann	Org. 1748
4	MS0892	Anthony Ross III	Org. 1748
1	MS1071	David Sandison	Org. 1740
4	MS1086	Wei Pan	Org. 1123
8	MS1415	Carlos Gutierrez	Org. 1114
4	MS1415	Taisuke Ohta	Org. 1114
4	MS1415	Thomas Beechem	Org. 1112
1	MS1421	Jerry Simmons	Org. 1120
4	MS9161	Kevin McCarty	Org. 8656
1	MS0899	Technical Library	9536 (electronic copy)

For LDRD reports, add:

1	MS0359	D. Chavez, LDRD Office	1911
---	--------	------------------------	------

For Patent Caution reports, add:

1	MS0161	Legal Technology Transfer Center	11500
---	--------	----------------------------------	-------





**Sandia National Laboratories**